In presenting this thesis in partial fulfillment of the requirements for an advanced degree at Idaho State University, I agree that the Library shall make it freely available for inspection. I further state that permission to download and/or print my thesis for scholarly purposes may be granted by the Dean of the Graduate School, Dean of my academic division, or by the University Librarian. It is understood that any copying or publication of this thesis for financial gain shall not be allowed without my written permission.

Signature _____

Date _____

An Investigation of Shielding Configurations for NaI Detectors in Standoff Applications

A Thesis presented by

Benjamin N. Satterwhite

to

The Department of Physics

in partial fulfillment of the requirements

for the degree of

M.S.

in the subject of

Applied Physics

Idaho State University

May 2014

To the Graduate Faculty:

The members of the committee appointed to examine the thesis of Benjamin N. Satterwhite find it satisfactory and recommend that it be accepted.

_____
Major Advisor: Dr. Alan W. Hunt

_____
Committee Member: Dr. Erdinch Tatar

_____
Graduate Faculty Representative: Dr. Dennis Stowe

Dedication

This thesis is dedicated to my parents, Janet and Larry Satterwhite, who have inspired a love of learning and life in me, for which I will always be grateful.

Acknowledgments

My greatest appreciation must be extended to the following remarkable people: Dr. Alan Hunt, Edna Cardenas, Mike Smith, Ed Reedy, Heather Siepel, the IAC engineering crew, Dr. Bob Mayo, Dr. Brian Fisher, and Dr. Doug Wells.

Contents

List of Figures

Thesis advisor
Dr. Alan Hunt

Author
Benjamin N. Satterwhite

An Investigation of Shielding Configurations for NaI Detectors in Standoff Applications

Abstract

Standoff detection of fissile materials has become a growing facet in a myriad of nuclear science applications. The presented standoff measurements utilized a 21 MeV photon beam produced by a linear accelerator(PITAS) to induce fission processes within desired material at distances greater than ~10 meters from the accelerating structure. Photofission decay processes within the inspection material produces unique γ-ray and neutron signals allowing fissile material detection. Unfortunately, significant signals can also be produced through neutron absorption within the experimental apparatus decreasing detection sensitivity. This thesis presents shielding configuration investigations for sodium iodide scintillation γ-ray detectors utilized in standoff measurements performed at the Idaho Accelerator Center airport facility. The primary focus of shielding configuration performance was to reduce activation as a result of neutron absorption within sodium iodide scintillation crystals. Multiple shielding configurations consisting of 5% borated polyethylene and cadmium were investigated for activation signal reduction within a bistatic detector configuration. Optimal shielding configurations were implemented in a large sodium iodide detector array.

Chapter 1

Introduction

1.1 An Argument for Standoff Detection

In the last decade, military strategies have placed greater emphasis on the identification of weapons of mass destruction [1]. Therefore, the ability to detect fissile materials has become a new facet in defense research. Efforts have focused on developing techniques to detect fissile material at distances greater than approximately 10 meters. While the apparatus and experimental strategy may change, the general principles of active standoff detection revolve around three main components: (1) creating a detectable signal from inspection object material, (2) measuring the produced signals by utilizing a detector apparatus, (3) analyzing the signal captured by the detector apparatus to determine positive or negative detection with a quantitative confidence. Significant proof of concept work has been done in all three areas, however, a large scale standoff detection system has yet to show confident detection of fissile material at substantial distances [3, 11, 8]. This thesis presents results for detection system optimization experiments, focused on shielding scintillation detectors from energy deposition specifically associated with neutron absorption. Experimental results were implemented by collaborators at Johns Hopkins University Applied Physics Laboratory to produce a standoff detector comprised of 16 sodium iodide(NaI) scintillation detectors consistent with detectors ustilized in Idaho Accelerator Center campaigns. Additional campaigns were then completed in the Spring of 2013 to test

the system's standoff detection capabilities. Understanding the methods of standoff detection and specifically active interrogation requires a thorough discussion of several nuclear physics topics.

1.2 Fundamentals of Standoff Detection

Utilizing the three basic components of active standoff detection as a guide, discussions begin with the creation of the detectable signal. Fission, or the splitting of nuclei into two (and sometimes more) daughter fission fragments, occurs in two modes: spontaneous fission and induced fission. Spontaneous fission occurs with generally heavy unstable nuclei without any outside perturbation. In contrast, induced fission splits heavy nuclei into fission fragments through the introduction of some external perturbation [10]. In this study, fission is induced by perturbing nuclei with high-energy($\sim$21 MeV) photons produced by a linear accelerator system, PITAS (Photonuclear Inspection of Threat and Analysis System). Energetic photons are absorbed into target material nuclei causing nucleon vibrations to increase. With enough energy, nucleon oscillations can pull the nucleus apart, leaving two separate daughter nuclei or fission fragments. Further discussions of nuclear structure are required to fully understand mass distributions of fission fragments as well as nuclear processes leading to fission. However, to understand the creation of detectable signals, one must look past the intricate mechanics of fission and focus on the decay chains of the fission fragments.

Fission fragments produced by fission reactions are often unstable and undergo characteristic decay chains to more stable isomers. Within these decay processes multiple signatures are produced and it is up to the discretion of the experimentalist and their apparatus as to which signature will be sought. While the time line of prompt neutrons and delayed signatures will be discussed in later sections, the focus of this detection system is to measure the increased yield of delayed γ-rays within a 3 MeV to 6.5 MeV energy region after a 250 ms time delay post radiation. There are advantages and disadvantages to all detectable signature schemes, but focusing only on the delayed γ-ray signatures allows for greater depth to be taken in understanding

optimum detector performance. To fully examine the delayed γ-ray signature, a foundation in particle detection will be presented.

Particle detectors are as vast in form as they are in function. In general, detectors rely on particle interactions with detector material to produce measurable effects attributed to individual particles. Presented in this study, NaI crystals provide reliable particle detection through scintillation processes within the detector material. Scintillation is a phenomena that has been integral in nuclear physics since the late 1940's [7]. Incoming particles are absorbed by atoms in the detector crystal, exciting electrons into higher shells then release excess energy in the form of visible photons. Visible photons are then collected by a photomultiplier tube (PMT), converted to electrons, and amplified for use in signal processing electronics. While the particulars of the system used will be fully described in a discussion of the experimental apparatus, signal detection begins with assessing known problems of nuclear detector physics.

1.3 Active Interrogation: The Problems at Hand

Detection of nuclear materials can be performed by two distinct strategies, passive measurements and active measurements. Although, passive measurements of fissile materials can show the existence of a fissile inspection object, many complications accompany passive detection strategies. Time duration, insufficient distance capability and an inability to identify inspection object material, all contribute to passive interrogation's lack of applicability in standoff detection systems. In contrast, active interrogation methods i.e. producing a measurable signal by inducing fission or other detectable decay processes, can provide detectable signals in short periods of time and more importantly, have a greater probability of detection at large distances. Unfortunately, active interrogation is not without its own unique set of complications [11]. Many detectors are unable to detect signals from a inspection object while the accelerator is emitting a photon beam, requiring the employment of time structured inspection methods. Furthermore, the addition of an interrogating device can complicate the detection process by adding unwanted signals produced by activation of

the experimental environment. Conveniently, shielding configurations can be used to significantly reduce the risk of detector activation.

While seemingly obvious, understanding one's environmental surroundings is important to all aspects of observation. The passive background is the signal received from the environment around the detecting apparatus. Contributions can come from local soils, building materials, cosmic particle interactions and even decaying isotopes in scientists. Passive backgrounds are easiest understood as the base line signal received from simply turning detectors on and seeing what they collect. Therefore, when an active measurement is taken, detectors will not only see the passive background measured when the accelerator is off, but additionally, all the low energy(0-100 keV) photon interactions and the signal produced by the target material as well. Not understanding environmental signals can distort and even hide important information in interrogation measurements. Any signal measured from a desired target must be statistically above the passive background to be detected and the introduction of an active interrogation scheme requires even greater scrutiny to background measurements. As a result, shielding configurations that can suppress passive backgrounds increase the sensitivity and accuracy of standoff detection capabilities, possibly allowing for longer standoff distances. However, caution must be applied to shielding methods for fear of shielding out the desired measurable inspection object signal. Shielding configurations can range from active shielding processes often seen in large scale cosmic ray observations, to the more readily available passive shielding methods of lead, polyethylene and cadmium employed in this study. Shielding configurations can be optimized not only for background mitigation, but also dictate what energy of incoming particles a detector may be exposed to. Similarly, shielding can provide assurances in the performance of detectors by limiting the possible activation of the detector apparatus.

Activation of local environments caused by exposure to high energy photons and neutrons can cause increases in particle detection rates, adding to the active signal of the accelerator and in the worst scenarios, drowning the desired signature of the inspection object. Due to the vast amount of photons leaving the beam line, an array of interactions can occur as photons interact with matter in the local environment. As

photons are absorbed and re-emitted or scattered, (γ,n) interactions can knock out neutrons that can then be absorbed in all components of the experimental apparatus. Activation concerns can be counterintuitive, as the primary objective for producing high energy photons is to have them be absorbed in inspection object material, resulting in the induced fission signatures desired for standoff detection. However, photon absorption, and more aptly, neutron absorption can create radionuclides which may take hours or even days to decay to pre-interrogation levels. Decaying isotopes can then release particles during an interrogation measurement, increasing the amount of particles detected. Particle detection that does not pertain directly to fission signals and the local passive background can effect the sensitivity and accuracy of standoff measurements. Similar to background mitigation shielding strategies, shielding methods can prevent the ability for stray neutrons to be absorbed within the detector crystals. The following experimental campaign attempts to address optimum shielding configurations for NaI detectors. All experiments were conducted at the Idaho Accelerator Center airport facility with the use of the PITAS accelerator system.

1.4 Experimental Apparatus and Campaign

Standoff detection research seeks to push the physical distances with which one can accurately and confidently detect fissile material. Therefore, it is natural that any testing environment must be able to accommodate not only an active interrogation system, but facilitate a wide range of detector configurations and distances. The Idaho Accelerator Center (IAC), a research facility in South East Idaho, allows for both aspects of active interrogation measurements. Housing the principle accelerator for these studies, PITAS, the IAC airport facility allows for a high energy (¿1 MeV) beam of photons ($\backsim$ 25 MeV) to be directed into an open air range with maximum distances of 125 meters down range and 150 meters cross range. PITAS is a linear accelerator that is capable of producing a bremsstrahlung beam of photons with a remarkable array of beam parameters. Operators provided by the IAC are able to use PITAS in different pulsed configurations. Variation within pulse structures allow for

customization of interrogation search methods. While beyond the scope of this thesis, the process of pulsing a bremsstrahlung beam in such a manner to best obtain fission fragment decay signatures is an extensive question of utmost importance. Currently, the preferred pulse structure for standoff measurements, including results presented in this thesis, is a 1 second on / 1 second off inspection cycle. Discussion of pulse structure will be saved for later sections, but the main purpose of on/off cycle created by the PITAS system is to irradiate targets for a certain period (1 second on) and almost immediately follow with a detection period (1 second off) allowing detectors to measure the decay chains of fission fragments created within the "on" portion. Further time constraints are placed on standoff signal measurements by delaying another 250 ms to allow for neutron thermalization within the experimental environment. These on and off inspection cycles are continued for a period of approximately 10 minutes. For each shielding configuration tested, a number of measurements were taken to analyze activation issues of detectors, as well as monitor passive background levels.

Experimental campaigns provide first hand measurement opportunities to better understand theorized shielding configurations. For the presented study, three identical St. Gobain NaI scintillation detectors were used. One detector was treated as a control and was removed from all active measurements and received no shielding. Using a control detector provides a baseline un-activated passive background to compare with detectors present in the active measurements. Detectors present in the active measurements were separated into shielded and unshielded configurations. By leaving one detector bare at all times, comparisons of activation levels between shielded and control detectors were possible. Problems did exist in some measurements, as shielding configurations that lacked the thickness to protect against activation allowed some neutron absorption within the detector crystal. As discussed in previous sections, multiple shielding configurations were used, including combinations of borated polyethylene, lead, and thin layers of cadmium.

1.5 Results and the Future

In the Fall of 2012, an experimental campaign explored the best possible shielding to address concerns of activation within the experimental environment. Accompanied with this motivation was a desire to provide not only an accurate assessment of shielding requirements, but also to recommend shielding configurations for the utilitarian purpose of the detector itself. Aspects of detector panel design required consideration, as weight and cost were large factors in the successful detector array design. Experimental campaign results did yield an optimum shielding configuration of 4 inches of borated polyethylene with a thin (1-2 mm) cadmium layer. However, considerations of cost and unfriendly usability required the cadmium to be removed from final panel design. Campaign measurements showed significant activation in the unshielded detector, with only minimal levels of activation observed in the shielded detector. These results gave greater validity to certain detector configurations that require a close proximity to accelerating structures. Furthermore, measurements were made to establish a base line for proper thickness of polyethylene shielding, with further consideration of weight restricting the thickness to around 4 inches. Upon construction, 4 inches of borated polyethylene proved to be a significant deterrent from activation, allowing for standoff detection at distances greater than 25 meters. These experimental campaigns and results will be presented in this thesis in conjunction with a background of fundamental physics principles with an emphasis in the following areas:

- The Physics of Active Interrogation Beginning with an overview of accelerator physics, physics fundamentals are presented for bremsstrahlung beam production, induced fission signatures and scintillation detector mechanics.
- Background and Detector Activation Characterization of environmental background signals and detector activation providing foundations for shielding configurations tested in experimental campaigns.
- Shielding Configurations Analysis of passive shielding methods implemented in experimental campaigns. Shielding configurations were tested for reduction

detector activation and applicability to long distance standoff measurements.

- Experimental Campaign Results Description and results of experimental campaigns are presented. Final results provided for optimum shielding configurations are then analyzed for use in large scale detector shielding.

Chapter 2

Physics Fundamentals

2.1 Accelerator Basics

Accelerators are emerging as a new tool in a myriad of research and public sector applications. As access to these machines increases, greater creativity may bring accelerator science into a new realm of opportunity. The technical complexities of accelerators cause each machine to be different, therefore, the presented work will be focused on RF electron linear accelerating systems similar to those first purposed by Wideroë in 1928 [4].

Linear particle accelerators or linacs accelerate charged sub-atomic particles through a linear chain of resonant cavities by utilizing particle interactions with an electric field, provided by a standing wave produced from a large radio frequency generator. Linacs can be distinguished by what kind of particles they accelerate and the amount of energy particles acquire within the accelerating structure. Within a linear electron accelerator, electrons are produced by a cathode that injects electron(s) into the first of many spherical resonant cavities carrying a radio frequency. The radio frequency(RF) generator delivers a wave that is tuned to the spatial dimensions of the cavities and causes electrons to accelerate through resonant cavities. Accelerated electrons exit the vacuum chamber through a thin window into the environment to bombard a photon radiator creating a beam of bremsstrahlung photons. If a beam of photons is produced, it immediately begins to interact with the environment. It is

easy to imagine accelerating systems becoming increasingly complex as multiple beam lines, intricate bending magnets and cooling devices become more prevalent. However, robust knowledge of accelerator physics is not required to understand photon beam production, rather a discussion of accelerator components provides an ample frame work for interrogation methods used in this thesis.

2.1.1 Anatomy of an Accelerator

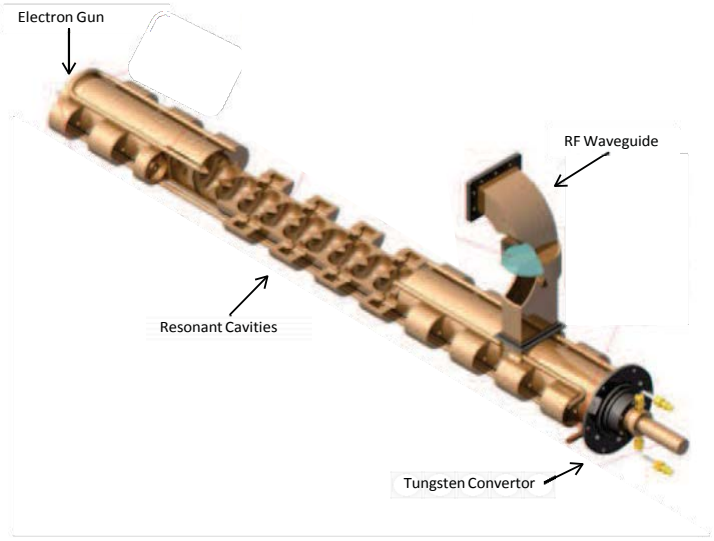

Figure 2.1: Schematic of Linear Accelerator. Components of an linear electron accelerator are depicted, including an electron source, resonant cavities, an RF waveguide and a bremsstrahlung converter.(Schematic use was authorized by its creator Mike Smith)

Illustrated in Figure 2.1 is a cut away schematic for a linear electron accelerator. Beginning with the left of the beam line assembly, at the entrance into the resonant cavities is an electron source. In the PITAS accelerator system, a thermionic triode electron grid gun is utilized to allow for greater versatility with beam pulse parameters. A more in-depth view of a general electron gun system is shown in Figure 2.2.

The triode gun utilizes an electron producing cathode and a “barrier” grid with a varying voltage potential to control the flow of electrons. By creating a barrier potential on the grid, an accelerator operator can control the electron current en-

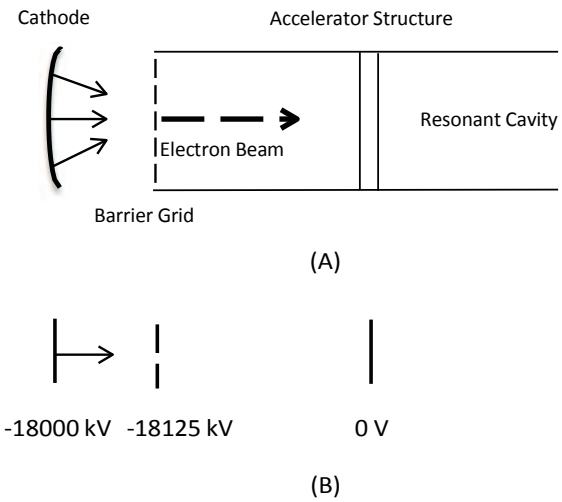

Figure 2.2: Schematic of Electron Gun. Electron sources produce electrons to be introduced to the accelerating environment. Schematic A is a physical representation of an electron gun, beginning with the electron producing cathode. Schematic B shows possible values for a barrier potential, trapping electrons, between grid and cathode before they can enter the accelerating structure.

tering the resonant cavities. Furthermore, the grid system allows for easier control of beam characteristics such as: pulse width, current and pulse charge. Electrons allowed past the barrier potential are repelled into the beam line by negative cathode potential focused toward the beam line by the concavity of the cathode. Once inside the accelerating structure, electrons are accelerated by a high energy electric field produced by the RF wave. High-power RF frequencies are produced by klystron RF amplifiers. Klystrons bunch electrons using an external low-energy RF generator, exciting microwaves of a desired frequency, and then directing them to the output of the klystron. High-frequency microwaves are then transported into the accelerating cavities by a waveguide, shown in Figure 2.1. The waveguide directs the RF wave into the resonant cavities where the frequency must be finely tuned to the spatial dimensions of the cavities. Electrons are accelerated through the resonant cavities by the electric field produced by the RF wave. As electrons leave the resonance cavities, they enter into an evacuated beam line assembly, leading to a bremsstrahlung radiator.

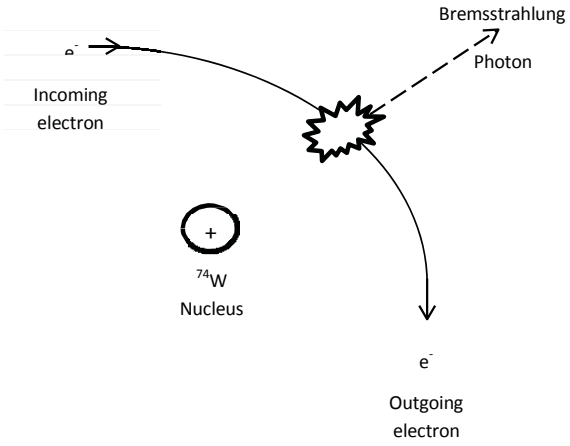

Figure 2.3: Bremsstrahlung Interaction. As the incoming electron's trajectory is bent, resulting radiation is released in the form of an energetic photon(Brem Photon).

2.1.2 Bremsstrahlung Photon Beam

Bremsstrahlung photon beams are created by bombarding a piece of dense material with high-energy electrons. However, accelerators are not required for bremsstrahlung radiation to occur, in fact bremsstrahlung is responsible for a myriad of de-acceleration processes. Tungsten is an optimum bremsstrahlung radiator due to its extremely high melting point and density, 3695K and 19.25 $g \cdot cm^{-3}$ respectively [2]. The high melting point protects the radiator from the immense amount of thermal energy deposited by the electron beam and a large density guarantees significant electron interactions will occur. Shown in Figure 2.3, an incoming electron interacts with the the Coulomb field of the nucleus, altering the electron's trajectory causing a release of radiation in the form of a photon, a process known a bremsstrahlung.

However, energy loss of incoming electrons can also occur through ionizing electron interactions or bremsstrahlung processes. Comparisons of ionization and radiation energy loss as a function of incoming electron energy are shown in Figure 2.4. Total energy loss becomes dominated by bremsstrahlung processes beyond the critical energy of 10 MeV. Resulting bremsstrahlung photons will carry energies proportional to the initial energy of incoming electrons [5]. This proportionality insures the energy of accelerated electrons is carried by the bremsstrahlung photon beam. While

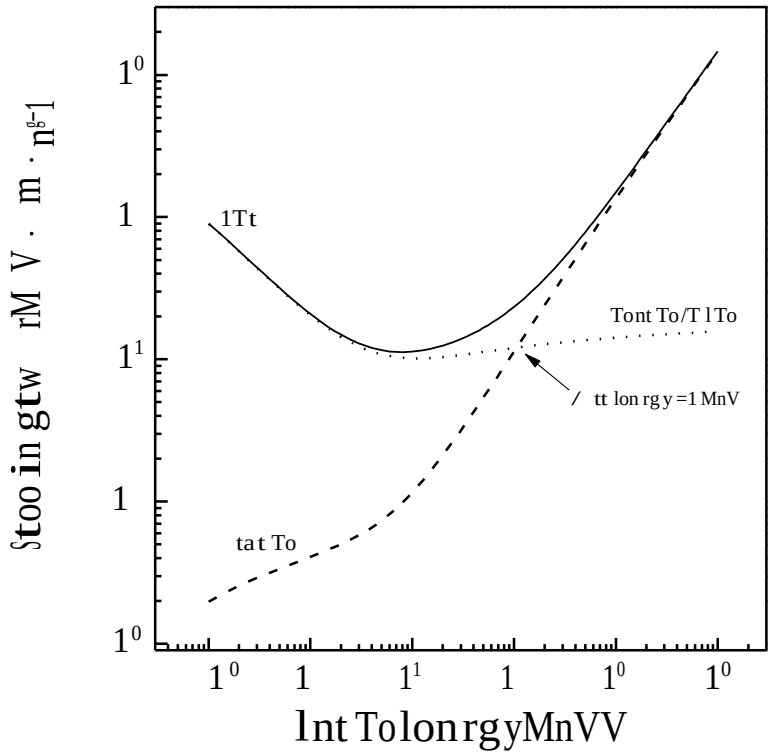

Figure 2.4: Stopping Power of Tungsten. Stopping power of tungsten bremsstrahlung radiator. As incoming electron energy increases, electron energy loss becomes dominated by bremsstrahlung processes.

not a necessity, collimation can suppress radiation produced around the accelerating apparatus and can narrow the beam of radiated photons as seen in the Figure 2.5. Once a photon beam is created, photons will begin to interact with all aspects of the experimental apparatus contributing significantly to the active background signal received during active standoff measurements.

2.2 Photon Interactions with Matter

The primary objective of producing a high-energy photon beam is to induce fission through photon and neutron absorption in the desired inspection object. However, photon interactions are not limited to induced fission interactions within inspection object material. Low energy(0-100 keV) photons will interact with matter through

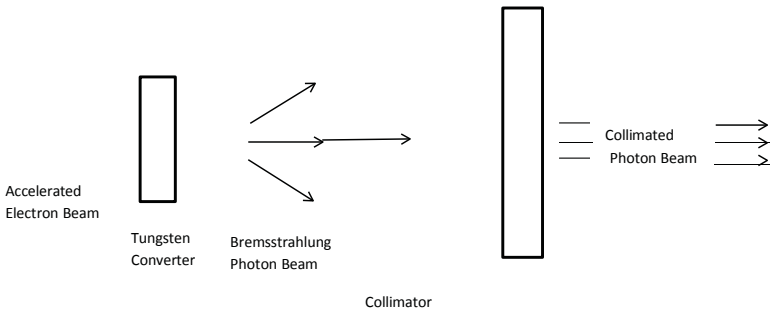

Figure 2.5: Bremsstrahlung Beam Production. An accelerated beam of electrons interacts with a bremsstrahlung converter. The bremsstrahlung photon beam travels through a collimator, restricting the beam and reducing radioactive dose in environments near the accelerator.

three main processes: the Photoelectric Effect, Compton Scattering and Pair Production. Shown in Figure 2.6, the photon attenuation for a ^{238}U inspection object is shown as a function of incoming photon energy. As photon energy increases photon attenuation becomes dominated first by Photoelectric effect, then Compton scattering and finally by Pair Production.

2.2.1 Photoelectric Effect

The photoelectric effect is the primary process for low-energy photon interactions. As photons interact with a material's atomic structure, photons can be absorbed by the electron cloud causing an electron to be emitted from the atom. The photoelectric effect requires the energy of the incoming photon (E_i) to be greater than the binding energy of emitted electron, known as the photoelectron. Shown below, the energy of the emitted photoelectrons, E_p, is equal to the energy of the incoming photon without the binding energy required to release the electron from its orbital shell, E_b.

$$E_p = E_i - E_b \tag{2.1}$$

Further de-excitation processes can occur after the photoelectron is emitted through the release of an x-ray or auger electron. In the first case, the hole left from the photoelectron is filled by an electron in an outer shell, as the replacement electron drops

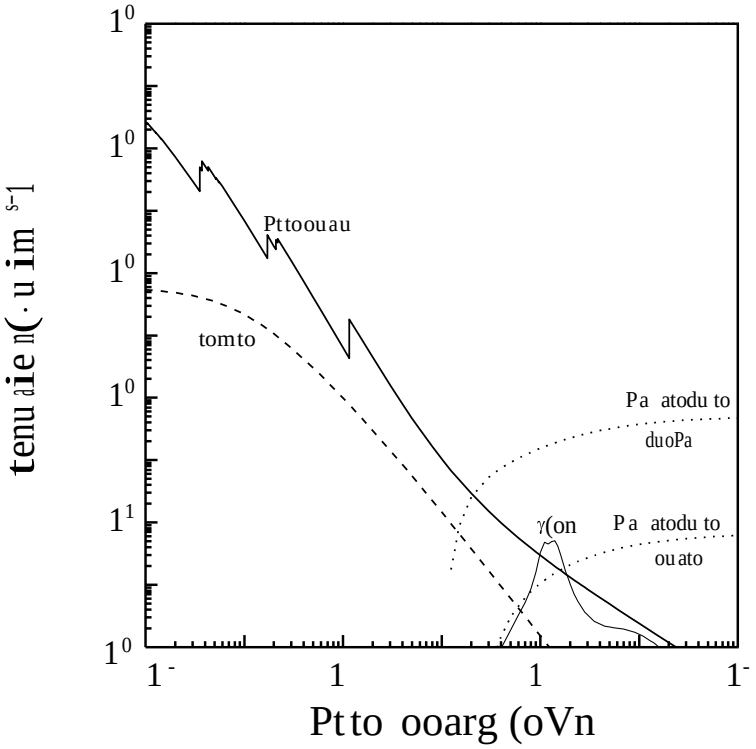

Figure 2.6: Photon Attenuation. Photon power of ^{238}U is displayed as a function of photon energy. Photon interactions are energy dependent, low-energy realms are dominated photoelectric effect. As photon energy is increased Compton scattering and pair production become the dominant processes of photon attenuation.

in to the vacancy an x-ray is emitted. In contrast, during Auger electron emission, the photoelectron vacancy is filled by rearranging electrons resulting in a second electron, the Auger or K-shell electron, to be emitted from the atom. The energy of the incoming photon is now split between the binding energy required to eject the photoelectron and the energy held by the relaxing X-ray or Auger electron. The photoelectric effect is the dominate form of photon interaction for photon energies below ~100 keV, and therefore, contributes to the low-energy signals obtained in active interrogation measurements. For energies between ~100 keV and ~ 1 MeV, photon interactions become dominated by Compton scattering.

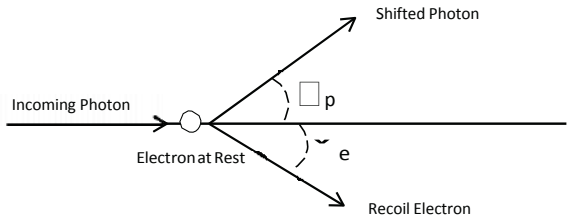

Figure 2.7: Compton Scatter Schematic. A general view of Compton scattering by a free electron at rest. An incoming photon is scattered off of an atomic electron, shifting the wavelength of photon and transferring energy to the free electron. Both particles are then scattered at different trajectories, θ_p and φ_e.

2.2.2 Compton Scattering

To first order approximations, Compton scattering of photons can be represented as a scattering interaction with a free electron at rest. The rest electron recoils from transferred energy given by the photon at an angle φ_e, while the incoming photon is scattered at an angle θ_p shown in Figure 2.7. Depending on scattering angle, the wavelength of the photon will be shifted proportionally with the relationship

$$\Delta\lambda_p \equiv \lambda - \lambda' = \frac{h}{m_e c}(1 - \cos\theta_p). \tag{2.2}$$

The shift in photon wavelength, $\Delta\lambda_p$, is proportional to the the cosine of the photon's scattering angle θ_p. In the presented equation, the wavelength of an electron is represented by the Planks constant, h, divided by the product of the mass of an electron m_e and the speed of light, c. Variation in scattering angles provide a spectrum of resulting wavelengths

For example, a head on collision, $\theta_p = \pi$, can result in the transfer of almost all incoming photon energy to the rest electron. In contrast, photons with small scattering angles, $\theta_p \approx 0$, will retain a majority of their initial energy. The variation of Compton scattering is an important representation of the cascading process seen throughout the experimental environment. Scattered photons with reduced energies will interact later with detector material or other components of the experimental environment, undergoing further photon interactions until the energy of the incoming photon is low enough for full absorption.

2.2.3 Pair Production

Pair production is a high-energy photon interaction that produces a charged particle pair within the interacting material. While pair production can refer to production of any particle and anti-particle pair, the conversion of a high energy photons to an electron-positron pair is most pertinent for this thesis. In contrast to previously described photon interactions, pair production has a determined energy threshold required for the creation of a electron-positron pair. Photons are massless particles, therefore, to create two mass particles, a significant amount of energy must be converted to mass abiding by Einstein's famous mass-energy equation. To create a electron-positron pair, the incoming energy of the photon, E_i must be greater than the rest mass of the two produced particles, namely, twice the mass of an electron (to account for the positron), m_e, multiplied by the square of the speed of light(c), as seen below

$$E_i \geq 2m_e c^2 \geq 1.02 MeV. \tag{2.3}$$

Incoming photons of appropriately high-energy can cause pair production through interactions with nuclei. Energy exceeding the 1.02 MeV threshold is transferred to kinetic energy of the electron-positron pair. Both charged particles will continue to traverse material loosing energy through bremsstrahlung and other radiation processes. Electrons will continue to traverse the materials loosing energy until absorptions. Similarly, positrons will thermalize within material until the energy is low enough for positron annihilation with another electron, resulting in the release of two 511 keV γ-rays with opposite trajectories, γ-rays are subject to further photoelectric

and Compton interactions or could be detected during active interrogation measurements. Final photon beam interactions take place with the inspection object, and in correct conditions can produce the induced fission signatures sought in standoff measurements.

2.3 Fission

During fission, a nucleus can be split into two or three, separate nuclei, often unstable and subject to radioactive decay. Energy thresholds for fission to occur is best described using the liquid drop model of nuclear structure presented by Bohr [10]. The liquid drop model describes the decreases in binding energy due to nuclei deformation, but gives little insight to asymmetrical mass distributions of daughter isotopes. For understanding of mass distributions, employment of the shell model of nuclear structure is required. The shell model relates nucleon organization to the orbital shell levels of atomic electrons. Nuclei with one or both nucleon shells filled will be more stable resulting in greater nuclear binding energy.

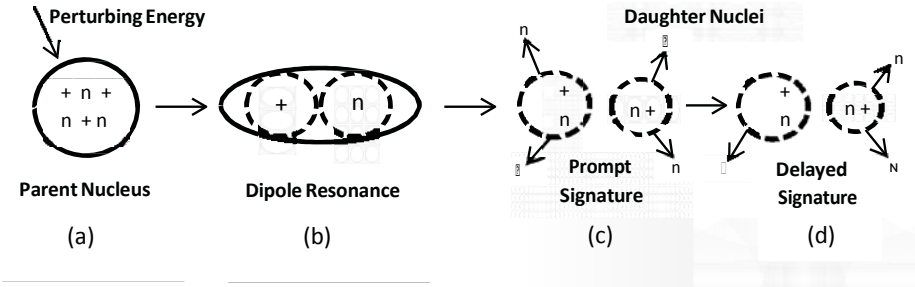

Figure 2.8: Fission Schematic. A fission process depicting perturbing radiation capable of inducing giant dipole resonances in parent nuclei. (a) The parent nucleus absorbs perturbing radiation, causing nucleon motion to increase(b). When scission of the nucleus occurs(c) a prompt signature of radiation is released in the form of neutrons and γ-rays. Daughter isotopes undergo further decay processes until a stable isomer is reached(d).

In Figure 2.8, the induced fission process is depicted beginning with the parent nucleus absorbing some form of perturbing energy (a). The nucleus absorbs the incoming particle's energy causing protons and neutrons to separate, forming a giant dipole resonance(b). Repulsive Coulomb interactions drive the nucleus apart, forming unstable fission fragments(c). Daughter nuclei decay to stable isotopes, releasing neutron and γ-ray signatures through β^- decay processes(d). Although, Figure 2.8 depicts the process for induced fission with perturbing energies within the region for

giant dipole resonances, particle energies within the GDR region are not required for fission to occur. The liquid drop model provides a physical representation for nuclear fission by describing nuclear structure through binding energy requirements.

2.3.1 The Liquid Drop Model and Nuclear Binding Energy

The liquid drop model is a physical representation of nuclear structure that assumes the nucleus to be an incompressible drop of liquid. When the nucleus is perturbed by incoming radiation nucleon motions increase, deforming the nucleus similar to the process depicted in Figure 2.8. If incoming radiation has energy within the region for induced fission, nucleon oscillations can split the nucleus apart, producing two or rarely, three daughter fission fragments. The liquid drop model gives a physical reference to the Weizerker nuclear binding energy equation(2.4) [10]. Nuclear binding energy (E_b) is the physical energy required to break a nucleus apart, and is a function of the number of nucleons A and the number of protons within the nucleus Z [10, 11, 8]

$$E_b = \alpha_1 A - \alpha_2 A^{2/3} - \alpha_3 \frac{Z(Z-1)}{A^{1/3}} - \alpha_4 \frac{(A-2Z)^2}{A} + \delta. \qquad (2.4)$$

Coefficients (α_n) are constants provided by standard data tables. The first term in equation 2.4 is the volume term and is proportional to the total number of nucleons within the nucleus. The volume term represents the force felt between all nucleons, assuming individual nucleons are surrounded on all sides. However, nucleons on the surface of the nucleus are not surrounded on all sides, requiring a correction term proportional to the surface area of the nucleus ($-A^{2/3}$) reflecting the decrease in binding energy. The third term in the nuclear binding energy is the Coulomb term($A^{-1/3}$). During fission processes the Coulomb repulsion of the protons drives the nucleus apart into fission fragments. Following the Coulomb term, the symmetry term(A^{-1}) represents all nuclei's preference to have equal number of protons and neutrons (N = Z). Finally, the δ term is dependent on even or odd numbers of nucleons and can decrease or increase binding energy depending on nucleon quantities.

For deformed nuclei, the liquid drop model reflects decreases in the nuclear bind-

ing energy due to changes in the surface and Coulomb terms of the binding energy formula. All other binding energy terms are constant throughout the deformation of the nucleus. In contrast, the surface area and Coulomb repulsion fluctuations depend on nuclear deformation. Therefore, when considering fission processes, binding energy approximations utilize only the surface area and Coulomb repulsion terms. As the nucleus is deformed, the surface area increases causing nucleons to be less bound and forces greater distance between protons, weakening Coulomb interactions. As binding energy decreases, heavier nuclei will tend to split, forming daughter fission fragments with cumulative binding energy greater than the binding energy of the deformed parent nucleus. Spontaneous fission requires the Coulomb repulsion between protons to overcome the strong force holding the nucleus together. Due to the dependence on the Coulomb repulsion, nature has a threshold of the number of protons required to have fission occur spontaneously. In equation 2.5, Z represents the total number of protons and A is the total number of nucleons within the nucleus.

$$\frac{Z^2}{A} > 47.8. \tag{2.5}$$

The above equation neglects quantum mechanical corrections for fission barrier tunneling, but still gives a good estimate for the spontaneous fission barrier. Spontaneous fission is observed in heavy elements, whose nuclei are more susceptible to internal perturbations, but spontaneous fission rates are unique for different heavy isotopes. Regardless of the perturbation's origins, scission of the nucleus often results in asymmetrical fission fragments. The liquid drop model is incapable of describing fluctuations in mass distributions of the fission fragments or increases in the nuclear binding energy for certain isotopes.

2.3.2 The Shell Model

The shell model treats nucleon structure similar to the orbital shells of atomic electron theory. Protons and neutrons fill respective shells within the nucleus in quantized energy steps obeying the Pauli Exclusion Principle. Similar to electron theory, nucleon shells with all positions filled are known to occupy "magic" states,

occurring at 2, 8, 20, 50, 82, 126 protons or neutrons. Magic states representing a full nucleon shell level are more stable than non-magic states, therefore, these states are preferred among nuclei. Furthermore, a "doubly magic" state can be formed when two nucleon shells are filled, as in $^{16}_{8}O_8$ with 8 protons and 8 neutrons. A simplified model of shell structure can be seen in Figure 2.9.

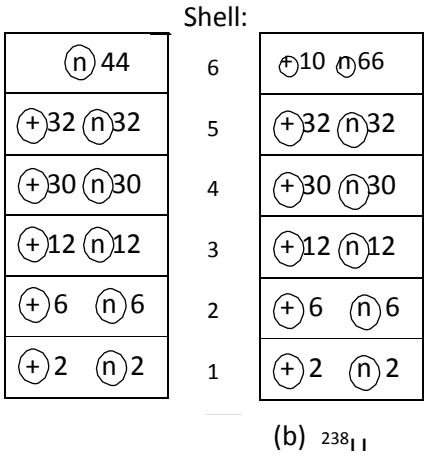

Figure 2.9: Shell Model Arrangement. Nucleon shell structures for (a) ^{208}Pb and (b) ^{238}U. The ^{208}Pb is a doubly magic isotope with 82 protons and 126 neutrons, in contrast, ^{238}U has neither neutron or proton outer shells filled.

Two example nuclei are depicted; (a) ^{208}Pb representing a doubly magic nuclei and (b)^{238}U with two partially filled shells. In this example, ^{208}Pb is an extremely stable isotope in comparison to ^{238}U that has partially filled shells and is susceptible to spontaneous fission. One of the final stable isotopes of the "radium" series, the ^{208}Pb doubly magic shell structure serves as a stable daughter product of heavier elements such as ^{238}U.

Nuclear shell structure and nuclei's preference to reside in energetically favorable states plays a direct role in the mass distributions of resulting fission fragments. Depicted in Figure 2.10 are the fission fragment mass distributions for ^{232}Th and ^{238}U. The low mass distribution shifts with the parent nuclei's nucleon abundance,(^{232}Th) $\sim$90 and (^{238}U) $\sim$101 respectively. In contrast, high mass fission fragment distributions stay relatively fixed at $\sim$140. The pinning of high mass distributions correlates

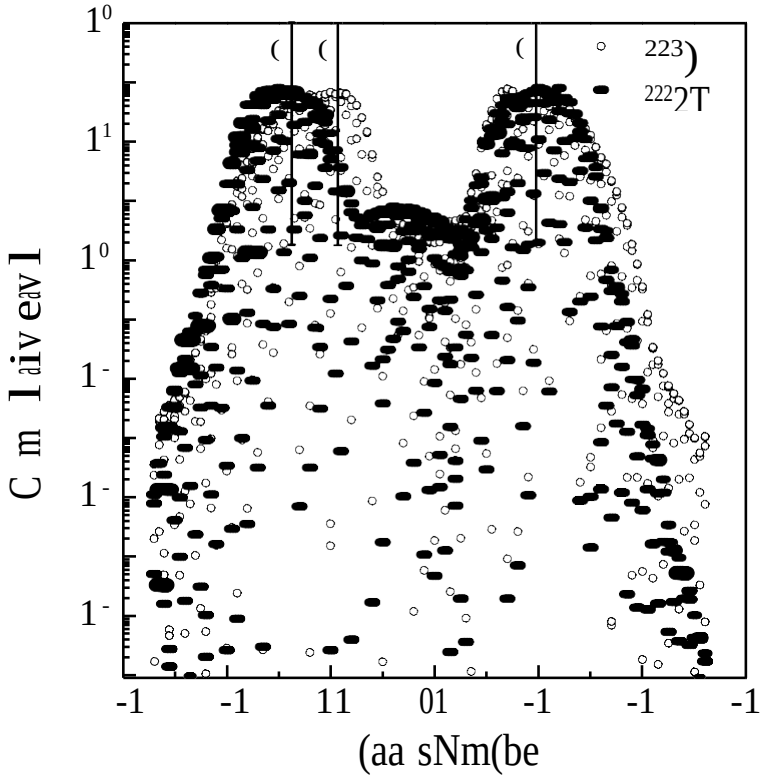

Figure 2.10: Fission Fragment Distributions. Induced fission fragment distributions for ^{232}Th(•) and ^{238}U(◦). The fluctuations of the centroid for low mass distributions correlates to parent nuclei(a/b). Stable high mass centroid is observed for both parent nuclei(c).

to doubly magic states with 50 protons and 82 neutrons (A=132). Additionally, a third distribution is visible in ^{232}Th fragment data, revealing that equal mass distributions are possible with proper perturbing energies. However, equal mass distributions result in unstable isotopes far from the "valley" of nuclide stability, making them energetically unlikely for most parent nuclei. High mass distributions will stay relatively constant regardless of parent nuclei, in contrast, lower mass fragments change with additional nucleons depending on parent nuclei structure. Although, the fission fragment distributions depend on the fissuring material, the probability of induced fission occurring relies further on the energy and the form of the perturbing radiation.

2.3.3 Neutron vs Photon Absorption

Unlike spontaneous fission, external perturbing radiation is used to induce fission in applicable inspection objects. Neutrons and photons do not have charge, and therefore, are not subject to Coulomb forces produced by the protons in the nucleus. Induced fission can occur by absorbing the energy of a photon or neutron into the nucleus in (γ,f) and (n,f) reactions. The following figures represent the cross sections or probability of fission taking place for both incoming photons and neutrons. Figure 2.11 shows the probability of neutron induced fission in ^{235}U and ^{238}U as a

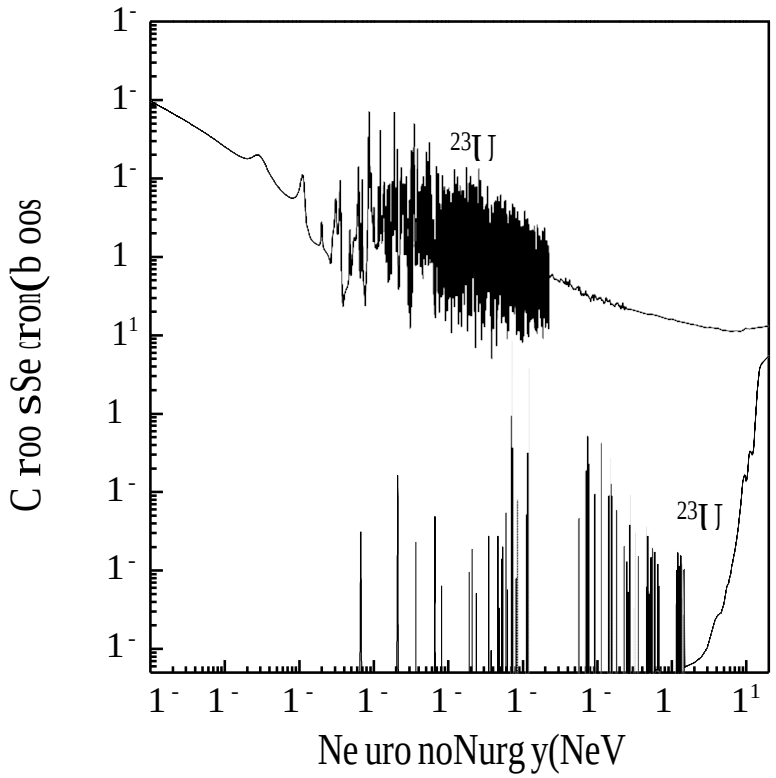

Figure 2.11: Neutron Induced Fission Cross-Section. Cross Sections for ^{235}U and ^{238}U are shown as a function of neutron energies.

function of incoming neutron energy. The cross section for ^{235}U is greatest in the thermal neutron range, in contrast, ^{238}U is not likely to fission until neutron energies reach ~1 MeV.

Comparatively, in Figure 2.12, photofission cross sections for the two targets do

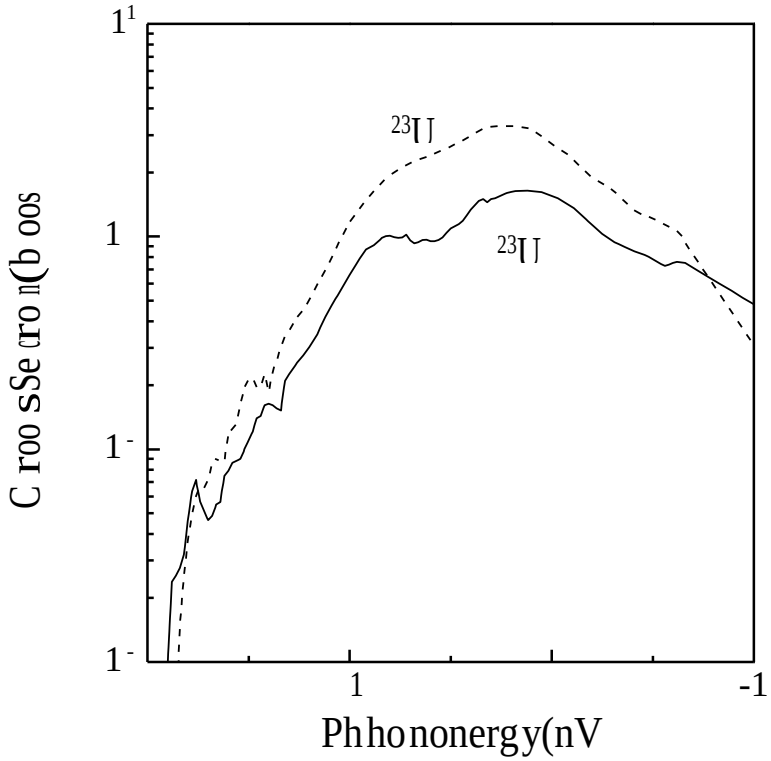

Figure 2.12: Photon Induced Fission Cross-Section. Cross Sections for ^{235}U and ^{238}U are shown as a function of inducing photon energy.

not increase to appreciable levels until incoming photons are ~5 MeV or greater. Photofission thresholds for both ^{235}U and ^{238}U are similar in shape, and represent the minimum photon energy required to break apart respective nuclei. Photofission cross sections reach a maximum for photon energies around ~14 MeV, coinciding with giant dipole resonance regions described in the liquid drop model. However, photon energies large enough to induce giant dipole resonances are not required for fission to occur. Nonetheless, once a parent nuclei is split, either through induced or spontaneous fission, fission fragments will produce consistent γ-ray signals through fission fragment decay.

2.3.4 Energy Release in Fission

Unstable fission fragments produce detectable signals through prompt and delayed decay processes. Returning to Figure 2.8, scission occurs after absorption of

the perturbing radiation,($\sim 10^{-21}$s) [11]. Immediately following scission, excited fragments emit prompt decay particles in the form of neutrons and γ-rays ($\sim 10^{-13}$s) [11]. Prompt decay emissions are then followed by delayed emissions from daughter nuclei decay processes. On average the energy released during a fission process is $\sim$200 MeV, but a majority of this is given to the kinetic energies of the fission fragments. Radiation released in prompt and delayed signatures are cumulatively less than $\sim$15 MeV [8]. A depiction of a possible decay scheme for neutron induced fission of a ^{235}U nucleus is seen below in equation(2.6)

$$^{235}U + n \rightarrow ^{236*} U \rightarrow ^{140} Xe + ^{94} Sr \rightarrow ^{140} Ce + ^{94} Zr. \qquad (2.6)$$

Prompt neutrons and γ-rays are released by excited ^{140}Xe and ^{94}Sr isotopes. Delayed signatures, consisting of β^- decay neutrons and γ-rays are released as ^{140}Xe and ^{94}Sr continue towards stable isomers. In equation 2.6, stable isotopes ^{140}Ce and ^{94}Zr are the final decay products of the depicted decay chain. While not all decay processes will be detected in standoff measurements, isotopes with longer half-lives may still produce delayed signals detected in later measurements. Multiple decay chains will ensue from the unstable nuclei, and the decay chain depicted above is one of many possible avenues of decay for the fission fragments of ^{235}U. Regardless of decay scheme, the prompt and delayed signatures released in the induced fission process are crucial for active standoff measurements.

However, the very signatures that standoff measurements seek, can contribute greater yields of extraneous low energy γ-rays within the detecting apparatus. Neutrons and γ-rays released in the prompt and delayed signatures are also subject to further interactions within the experimental environment. Neutrons emitted in the fission decay processes are free to thermalize within the local surroundings through (n,γ) interactions. These γ-rays are then readily available for detection within the detector apparatus. To account for the increase of γ-rays released within this thermalization period, further strategies must be implemented with the data analysis portion of standoff measurements. Furthermore, neutrons that are not absorbed within the experimental environment can be absorbed within the detector apparatus causing activation within detector crystals. Energy deposition through neutron absorption

can greatly affect the sensitivity of standoff measurements. Therefore, the mechanics of scintillation detection and activation through neutron absorption are of great importance.

2.4 Detector Mechanics and Activation

Particle detectors utilize charged particle interactions with detector materials to create measurable signals for amplifying electronics. Particle detectors used in nuclear physics applications are often chosen for desired particle interactions. Presented results are focused on delayed γ-ray signatures and therefore require detectors capable of measuring incoming γ-rays. Although, multiple detector materials are able to detect γ-rays the experimental results from this thesis are focused on NaI scintillation detectors. Therefore, the mechanics of scintillation within inorganic crystals and the detected signal's reliance on photomultiplier tubes will be presented. Scintillation fluorescence occurs when the energy of a charged particle is absorbed within detector material releasing energy as a visible photons. The visible photon is then collected by a Photomultiplier Tube (PMT), converting photons into electrons and then amplifying resulting electron pulses as they cascade down the dynode chain. Signals leaving the photo-multiplier are received by amplifying electronics discussed in the apparatus portion of this thesis. Detection is not isolated to induced fission signatures, rather all γ-rays that interact with detector material will contribute to the measured signal.

2.4.1 Scintillation in NaI detectors

Scintillation has been a corner stone of particle detection since the early 1900's. Scintillation can occur in a myriad of materials including organic and inorganic crystals. In general, scintillation begins when charged particles are absorbed by a material, exciting electrons into higher orbital shells. As atoms de-excite to pre-absorption energy levels, a visible photon is released for collection by an attached PMT. Scintillating materials can produce visible photons, such as the fluorescence screens used in early experiments. However, not all scintillating materials produce visible photons

ideal for PMT collection. Scintillating materials, such as NaI crystals, are unable to release visible photon light due to the distance between valence and conduction bands. Therefore, *activators* are used in conjunction with scintillating materials providing a secondary set of excitation levels. NaI detectors grown with traces of thallium were

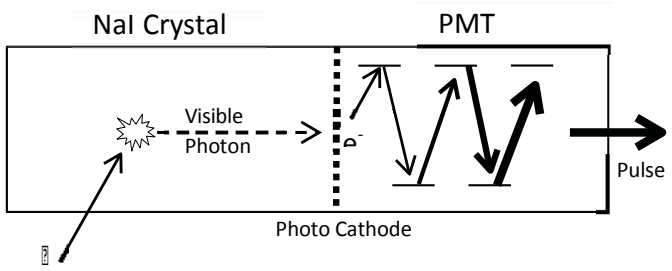

Figure 2.13: Scintillation Process. Scintillation occurs when γ-rays are absorbed, exciting electrons within the crystal lattice. As electrons relax to lower energy levels, a visible photon is released. Visible photons are collected and amplified by a photomultiplier tube.

first introduced by Robert Hoftstadter in 1948 [9]. Once an electron is excited into the conduction ban, as shown in Figure 2.14, energy released during de-excitation is greater than the energy ranges for visible photon emission. Traces of thallium are grown inside the NaI lattice structure to provide a secondary shell structure for excited electrons to relax into, with energy differences proportional to visible photons energies. Once emitted, the PMT collects the visible photon and converts it into an electron using a photocathode. The emitted visible photon hits a thin semiconducting photo cathode, absorbing the photon's energy and releasing an electron with energy proportional to that of the visible photon, a prime example of the photoelectric effect. The photocathode can carry a negative high voltage causing emitted electrons to be propelled towards a cascade of dynodes. Dynodes split the negative potential, causing electrons to travel through the dynode series towards the anode which is set to ground. Although, this voltage potential scheme is common, other PMT configurations exist. Regardless, dynodes have a high *secondary-electron emission coefficient*, causing

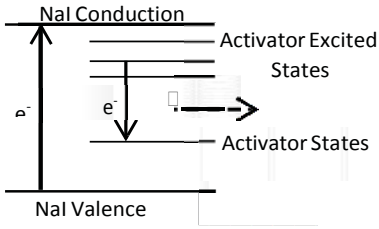

Figure 2.14: Activator Scintillation Levels. Electrons from NaI crystal are excited into the conduction band by incoming particles. Electrons relax into activator states rather than dropping back to the NaI valence shells. De-excitation within the activator states emits the photon of desired wavelength.

multiple electrons to be emitted upon initial electron interaction [7]. Secondary electron emissions amplify the electron pulse between each dynode. The signal, originally produced from initial scintillation interactions within a NaI crystal, exits the PMT through the anode to experimental electronics. The scintillation process is characterized above in Figure 2.13 beginning with the absorption of an incoming γ-ray.

2.4.2 Activation of Apparatus

Scintillation interactions within detector materials are not isolated to only desired signals. Rather, energetic neutrons produced through photon interactions with the experimental apparatus can be absorbed by nuclei in surrounding areas. Low-energy neutrons absorbed by nuclei can form radioisotopes with half-lives and decay products that are detrimental to measurement accuracy. Radioisotopes with large half-lives can affect the ability to produce accurate consecutive measurements, as decay products may last seconds to days after initial activation. Shown below are two possible decay chains of activated nuclei within the NaI detector crystal:

$$^{127}I + n \rightarrow ^{128}I + \gamma \rightarrow ^{128}Xe + \beta^{-} + \nu + \gamma... \quad (2.7)$$

$$^{23}Na + n \rightarrow ^{24}Na + \gamma \rightarrow ^{24}Mg + \beta^{-} + \nu + \gamma... \quad (2.8)$$

Equations 2.7 and 2.8 show excited isotopes created by neutron absorption in detector crystal nuclei. Naturally occurring ^{127}I in NaI crystals can absorb a neutron forming ^{128}I isotopes, releasing a 6.83 MeV γ-ray in the process. The ^{128}I isotope decays to ^{128}Xe through β^- emission with a half-life of 25 minutes. Other decay chains are possible, as 6.9 % of the time ^{128}I will decay to ^{128}Te. Similarly, ^{23}Na can absorb a neutron forming an unstable radioisotope ^{24}Na which in turn is subject to the decay processes shown in equation 2.8. Unlike ^{128}I, ^{24}Na decays to a single isotope ^{24}Mg, with a half life of $\sim$15 hours. When NaI detectors become activated, future measurements will detect the decays of these activated isotopes within the scintillating material. Therefore, measurements must sometimes be halted for multiple half life cycles to allow for detectors to return to pre-activation form. For example, the activation of ^{23}Na nuclei may require measurements to be delayed upwards of 45 hours to decrease activation counts to negligible levels.

In addition, all resulting decays have a maximum amount of released energy, including neutrinos and γ-rays shown in the final decay processes of equations 2.7 and 2.8. Known as the Q-value, the total energy released in a decay scheme can contribute undesired particles within the measurement region of interest. The presented measurement method rely on the increased particle yields of γ-rays within a 3 MeV - 6.5 MeV range. However, if activated nuclei can produce decay emissions within this range measurement accuracy can deteriorate quickly. The Q-value for ^{128}I is 2119 keV [6] and lies below the energy region of interest. In contrast, ^{24}Na has a Q-value of 5515.78 keV which can contribute to signals within the desired region [6].

2.4.3 Shielding

Shielding configurations can suppress background signals received by detectors and more importantly, reduce activation within detector material. Passive background signals can have a multitude of origins such as: cosmic radiation, constituent detector material and terrestrial radiation. In the presented campaign, cosmic and terrestrial radiation provide the greatest contributions to passive background signals when no inspection object is present. Cosmic radiation signals are created as

high-energy, charged particles interact with the upper atmosphere undergoing various scattering processes [9]. Scattered particles consisting of neutrinos, γ-rays, neutrons, electrons and muons continue towards Earth's surface, undergoing further scattering interactions with particles in the lower atmosphere. At sea level, muons make up 80% of charged particle flux, with an intensity of about one muon per cm^2 per minute [9]. In contrast, terrestrial radiation arises from the radioisotopes within the surrounding experimental environment. For example, potassium is found naturally in construction materials such as concrete. Natural potassium contains 0.012% ^{40}K, a radioisotope subject to β^- and γ-ray decay processes subject to detection [9].

Shielding configurations designed to suppress cosmic and terrestrial radiation require dense materials with high atomic numbers. Therefore, lead has become a standard for low-energy photon background suppression along with steel, concrete and tungsten. Lead has a large density (11.34 $g \cdot cm^{-3}$) and a high atomic mass (A=208), requiring thicknesses of only a few centimeters to provide large decreases in low-energy backgrounds. Similarly, concrete can provide significant background suppression, but due to a smaller density requires greater thicknesses. Furthermore, natural radioisotopes within concrete, such as ^{40}K, can provide additional signal contributions. Nonetheless, concrete can prove to be useful shielding material as long as active measurement yields are significantly greater than the signal produced from concrete impurities.

Neutron shielding requires a departure from low-energy background suppression strategies. High-energy neutrons must first be moderated within shielding materials, yielding low-energy thermal neutrons. Neutron moderators require light nuclei for better high-energy neutron moderation. Therefore, shielding materials containing significant amounts of hydrogen are the best neutron moderators. High-energy neutrons collide with hydrogen atoms, slowing down in inelastic collisions and reducing the energy of the neutrons in a process known as thermalization. As more collisions take place, neutrons loose enough energy to become absorbed within other nuclei. It is often advantageous to place neutron absorbers within the material itself, or as an internal layer between moderating materials and the detector. Polyethylene with a homogeneous mixture of boron was used as a neutron moderator. Boron has a high

cross section for thermal neutron absorption, and can easily be placed within moderating materials. However, neutrons with enough kinetic energy to travel through moderating material may require additional absorption layers. Neutron absorption materials such as cadmium, can be used inside neutron moderation materials to absorb thermal neutrons that have traverse the entire moderating material. Multiple shielding configurations were used to optimize the suppression of passive and active backgrounds while protecting detectors from neutron absorption based activation.

Chapter 3

Experiment

Experimental campaigns conducted in November of 2012 focused on the optimization of shielding configurations for NaI γ-ray scintillation detectors. Shielding configurations were designed to suppress passive background signals measured by scintillating NaI crystals, with a specific focus on undesired signals produced by detector activation. Shielding configurations consisted of varying thicknesses of borated polyethylene, used for neutron moderation, and thin layers of neutron absorbing materials such as cadmium. Campaign measurements utilized the Photofission Interrogation Threat Assessment System (PITAS) to produce pulsed bremsstrahlung beams at energy levels capable of inducing fission within inspection objects. Resulting γ-ray signals are detected by NaI scintillation detectors, and processed through a series of NIM electronics.

3.1 Environment

The Idaho Accelerator Center airport facility provides a unique open range experimental environment ideal for standoff measurements. The Idaho Accelerator Center(IAC) is a research facility in Southeast Idaho that performs accelerator based experimental research. Separate from its main experimental campus, the Idaho Accelerator Center airport facility is located near the Pocatello Idaho Regional Airport. The IAC airport facility houses PITAS, a $\sim$25 MeV linear accelerator system,

employed in standoff measurements. The PITAS system delivers a bremsstrahlung photon beam into an open air range with maximum interrogation distances of ~125 meters down range and ~150 meters cross range. A layout of the IAC airport facility is depicted below in Figure 3.1. The IAC airport facility is comprised of a large

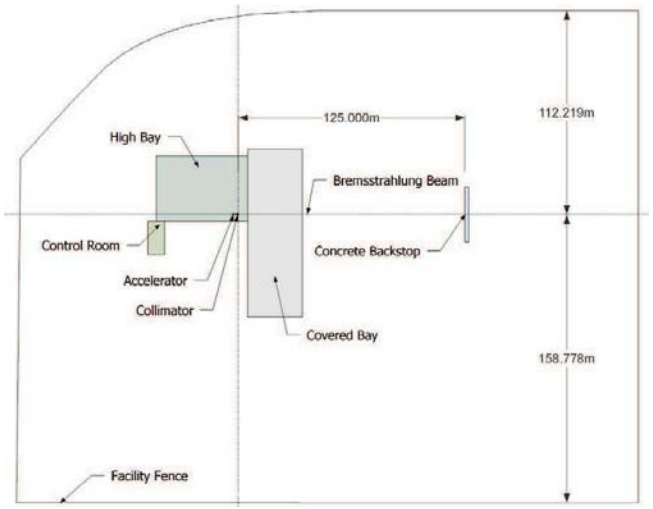

Figure 3.1: IAC Airport Facility. The open air range allows for both mono-static and bi-static detector configurations, providing measurement distance capabilities of 125 meters down range and 150 meters cross range.

high bay warehouse building with a covered open air hanger set within a large fenced compound. The PITAS accelerator inhabits the southwest corner of the warehouse, surrounded by significant concrete shielding designed to reduce radiation dosage in the immediate environment. Bremsstrahlung beams produced by the PITAS accelerator system are directed to the open air range, ending with a concrete beam stop at the far end of the facility. Within the open range, the detector apparatus can be placed in bi-static or mono-static configurations. Mono-static configurations attempt to orient detectors flush with the accelerating structure. In contrast, bi-static configurations align the detecting apparatus with inspection objects placed at a distance from the accelerator. The detecting apparatus is oriented at a cross range distance from the inspection object. Signals measured by the detector apparatus are sent through wireless connections to the experimental control room located in the Northwest corner of main facility warehouse.

3.2 Apparatus

3.2.1 PITAS

Active interrogation measurements seek to detect induced fission signatures produced in inspection objects. Therefore, discussion of the apparatus will begin with the source of inducing radiation, the PITAS accelerator system. PITAS utilizes a Varion 2500 linear electron accelerator capable of end-point bremsstrahlung energies of ~25 MeV. A klystron RF amplifier produces a 2.856 GHz S-Band wave directed by a wave guide into resonant cavities; accelerating electrons repelled into the resonant structure, seen below in Figure 3.2. Electrons are produced by a thermionic triode

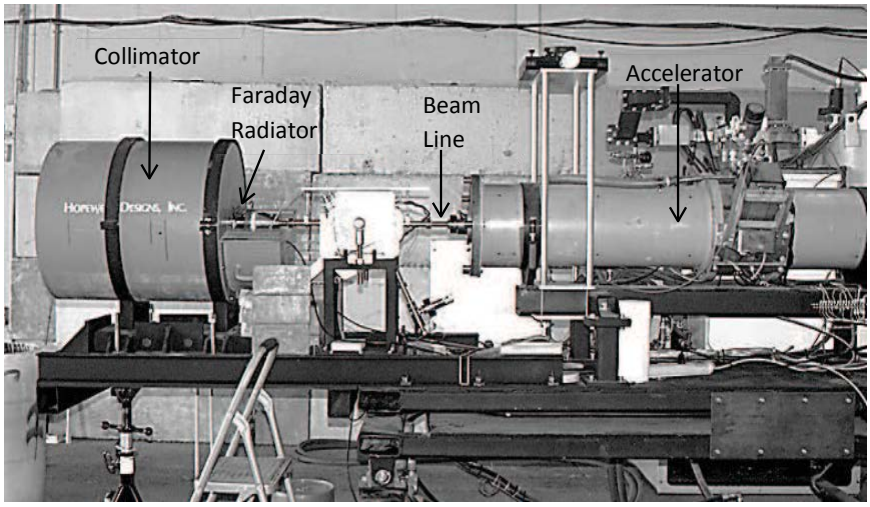

Figure 3.2: PITAS. The Photoelectric Interrogation Threat Assessment System is a linear accelerator system that produces bremsstrahlung photon beams for use in standoff detection measurements.

gun capable of producing electron pulses with widths of 200 ns to 4 μs shown in Figure 3.3a. Electron pulses exit through an evacuated beam line where it is measured by the first of two current measurement devices. Electron beam currents are measured by two devices, a Faraday cup placed within the bremsstrahlung radiator and a current transducer placed just before the aluminum bremsstrahlung radiator. Charge and current measurements as a function of end-point beam energy are shown in Figure 3.3b. Bremsstrahlung photons are produced as electrons leave the beam line

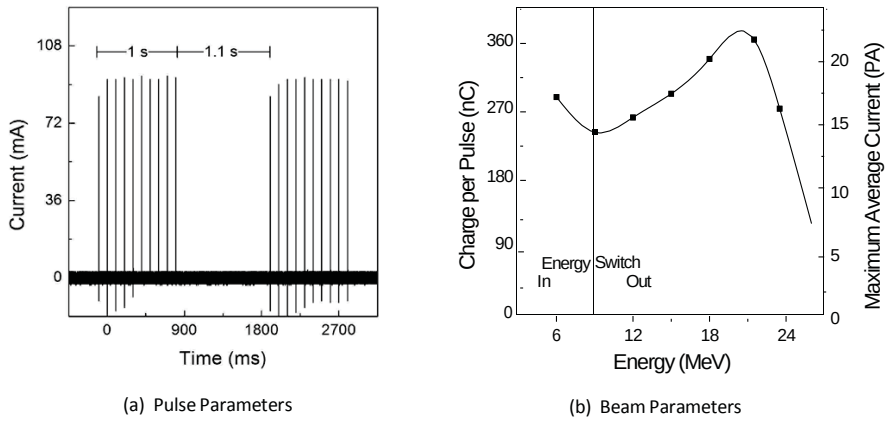

Figure 3.3: PITAS Beam Parameters. Pulsed photon beam parameters are shown for PITAS accelerator system. (a) A typical interrogation cycle for standoff detection measurements. (b) Beam current and pulse charge are shown as a function of end-point electron energy.

and interact with an aluminum bremsstrahlung radiator at the base of the collimator unit. The collimator unit consist of lead and water extended polyethylene materials to moderate and absorb scattered radiation from the accelerating structure. Once photons leave the beam line and pass through the collimator, photon interactions with the experimental environment and inspection objects produce signals for the detecting apparatus.

3.2.2 NaI Detectors

Standoff detection measurements taken in the experimental campaign utilized three NaI scintillation detectors. A model schematic of a 2X4H16 NaI detector crystal is shown in Figure 3.4. Crystal dimensions are presented yielding a detector surface area of 1.512×10^3 cm^2, utilizing 5 surface contributions neglecting the side holding the Photomultiplier tube. Scintillation occurs within the crystal, and visible photons with proper trajectories are collected by the attached 14 prong PMT with a positive voltage bias with a maximum operating voltage of ~1500 V. In the experimental campaign presented, the NaI detectors were operated at a 1100 Volts produced by an

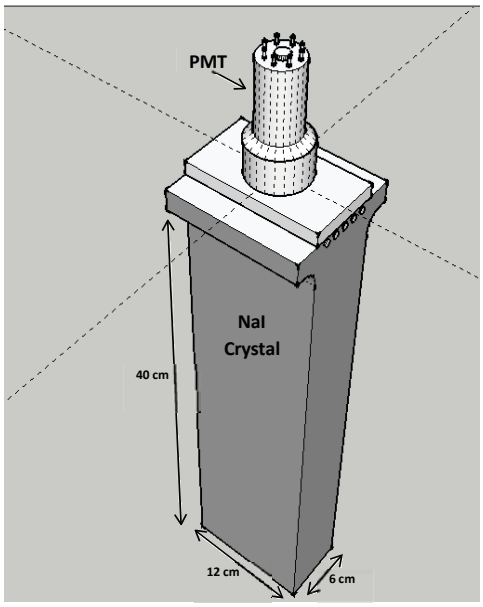

Figure 3.4: St. Gobain NaI Detector. Model number 2X4H16 were used to test optimum shielding configuration. Used primarily for γ-ray detection, NaI crystals are remarkably robust and can be grown to large dimensions.

high voltage power supply. Photomultiplier tube bases take detected signals, amplified by the PMT, and sends them into a BNC connecter cable to the first module in a series of electronics.

3.2.3 Electronics

Signals collected by the detector are not immediately prepared for data analysis. Measured signals must be amplified and manipulated through a series of electronic modules, and converted to a digital signal for computer interface. A schematic of the amplifying series is shown in Figure 3.5. Once a signal leaves the PMT base, the charges collected and amplified by the PMT are converted to proportional voltages by an preamplifier. Furthermore, with out preamplification the measured signal may be lost through attenuation processes within electronic cabling due to mismatched impedances between electronic modules. Signals leaving the preamplifiers are sent to an dual spectroscopy amplifier, providing a wide range of amplifying parameters that effect the pulse digitization. Specifically, manual adjustment of course and fine gain

Figure 3.5: Electronic Series. Scintillation signals produced by particle interactions travel through a series of electronic modules for computer interface hardware. Charge signals from PMT's are converted to proportional voltage signals by Ortec 113 preamplifier. Amplified signals are adjusted for energy calibrations by Ortec 855 Spectral Amplifiers. Amplified analog signals are then converted to digital signals for energy spectra software.

settings are required to place measured spectra within proper energy regions. Due to imperfections in NaI crystals, individual crystals have unique resolutions requiring different gain settings. Signals leaving spectral amplifiers are then sent through an Analog to Digital Converter or ADC. The ADC takes the analog signal produced by the amplifier and converts it to a digital signal usable by computer interface software. Settings for the ADC provides channel division designation for use in spectral analysis software. In the presented campaigns, spectral analysis was completed with 4096 energy channels. The ADC reads the respective peak height voltage of the measured signal and then assigns the signal to a particular channel. These "channel assignments" correlate to the energy deposited within the scintillation detector. Signals are then recorded by MPANT software, building a particle yield vs channel spectrum. Channels are assigned a particular energy based on morning calibrations with known radioisotopes.

3.3 Measurements

Measurements consisted of active interrogations (~10 minute) with inspection objects and longer passive measurements (~40 min) with no inspection objects present. Measurements utilized three St.Gobain scintillation detectors: NaI(1) was unshielded, NaI(2) was shielded, and NaI(3) was used as a control detector. NaI(1) and NaI(2)

were present for all active and passive measurements, providing comparison of activation and background suppression between different shielding configurations. The control detector, NaI(3), was removed for all active measurements and present for a majority of passive measurements. The control detector provided a baseline of non-activated background signals received during passive measurements. The control detector insured accurate activation comparisons with other detectors and monitored activation of immediate experimental apparatus such as the hydraulic table and data acquisition rack (DAQ). Detectors were placed in a bi-static configuration ~ 25 meters from the accelerator, with ~3 meter cross range distance between detectors and inspection objects. Active measurements were distinguished by inspection object material type consisting of Pb, ^{238}U and no inspection object measurements.

3.3.1 Detector Layout and Inspection Object Material

A picture of the experimental apparatus is shown below, the detector layout consisted of three NaI detectors, two BGO scintillation detectors and three ^{3}He ionization chambers. Utilizing other detector forms allows for greater comparison of NaI detector performance. The ^{3}He tubes function as neutron detectors while the BGO detectors measure γ-ray signature similar to those sought by NaI detectors. The BGO detectors mirrored the shielding configurations of the NaI detectors allowing for comparisons of detector efficiency. All detectors were placed on a hydraulic lift table, with consistent positions throughout the experimental campaign. All electronics were within the immediate environment of the detecting apparatus, and therefore, a wireless connection was utilized to start and stop measurements from the control room. Inspection objects were placed at a distance of ~25 meters from PITAS as shown in Figure 3.7. The detector apparatus was placed inside a tent for protection against outside elements encountered in the experimental environment. Cement barriers were used as shielding to protect electronics and detector apparatus from exposure to the bremsstrahlung beam. While activation is an important concern of the campaign, direct exposure to the PITAS beam can cause saturation within the detectors preventing detector operation regardless of crystal activation. Inspection objects

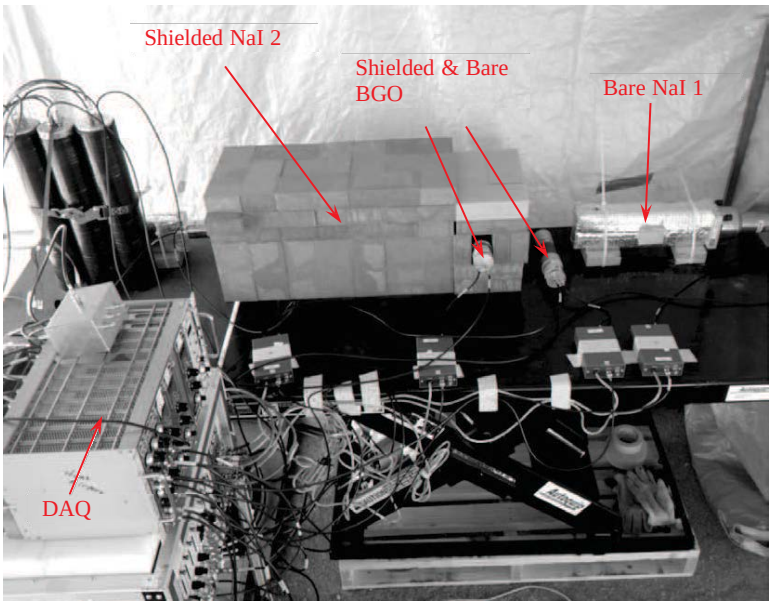

Figure 3.6: Experimental Apparatus Layout. Experimental apparatus for standoff measurements include shielded and un-shielded NaI and BGO detectors placed on an elevated hydraulic table. Data acquisition equipment is shown with NIM bin modules consisting of spec amps, power supplies, ADC's and MPANT software/hardwear. Not labeled are three ^{3}He ionization chambers and the control NaI detector.

consisted of single ^{238}U and Pb plates placed at a 45 degree angle with respect to detectors. Active measurements with the Pb inspection object allow for comparisons of signals produced during ^{238}U interrogations. Similarly, no inspection object(NOI) measurements were used to characterize the signal received during active measurements. During passive measurements, the ^{238}U inspection object was removed from the immediate experimental environment and the control detector was placed with the detector apparatus. As previously mentioned, the control detector was removed from the immediate experimental environment during active measurements.

3.3.2 Measurement Schedule

Reproducibility is of utmost importance in any experiment, therefore an attempt was made to keep the detector apparatus in near uniform conditions allowing reliable and reproducible performance. Initial campaign preparations were performed

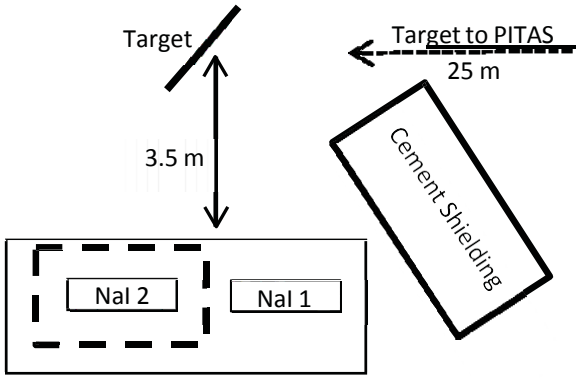

Figure 3.7: Bi-static Detector Layout. A detector apparatus placed in bi-static configurations ~3 meters from target material placed at 45 degree with respect to NaI detectors. Target material is placed ~25 meters down range from PITAS accelerator system.

on Monday, November 5, 2012, consisting of apparatus inventory. Following apparatus set-up, individual NaI detector parameters were addressed, including "pole zero", lower level discrimination, gain adjustments and zero crossings. Beginning with the pole zero, the unipolar signal from the amplifier was viewed on an oscilloscope and the pole zero is adjusted to minimize the undershoot/overshoot of the signal as it returns to baseline. After pole zero adjustments, the lower discriminator on the ADC is adjusted to set the lower limit energy of spectra, therefore insuring desired low-energy signals are measured. Following lower level limit adjustments, further detector parameters are adjusted through the use of known calibration sources.

Calibration sources provide a reliable decay signature from known amounts of radioisotopes and are used in particle detection for energy settings and calibration. A 10 μC ^{22}Na button source was used to set the spectrum's full energy range and minimize zero crossings within energy calibrations. The radioisotope ^{22}Na decays predominately by emitting two decay peaks, a γ-ray peak at 1274.5 keV and a positron annihilation peak at 511 keV. Reliable decay peaks can be utilized with gain adjustments to obtain desired energy ranges within the spectra. By raising the fine/course gains the bin width will increase and decrease, controlling the energy range of the

measured spectra. Therefore, if the total spectra has 4096 channels, and the 511 keV peak is directly in the middle of the spectra (channel 2048), the maximum energy possible within the spectra will be 1022 keV, resulting from a 2 keV per channel energy calibration. For this experimental campaigns a range of energy out to $\sim$7 MeV is desired to encompass the entire energy region of interest (3 MeV - 6.5 MeV), resulting in a 511 keV peak position around channel 295. Further use of the ^{22}Na source allows for a minimization of the spectrum's zero crossing, providing greater ease in spectrum comparison. Obtaining a large zero crossing on a single detector may require greater data analysis due to spectral shifts caused by the individual calibrations. Utilizing the two distinct peaks of ^{22}Na, a two-point calibration can be measured and adjusted depending on linear calibration fits seen in equation 3.1

$$E_\gamma = \Delta_{ch} C + z. \tag{3.1}$$

Equation 3.1 takes peak position centroid measurements, C, and correlates measurements to channel positions. Similar to linear line fitting, Δ_{ch} represents the slope value or energy per channel bin width, while z is the zero crossing. Large z values can be adjusted through use of zero controls on ADC modules. Unfortunately, sensitivities in the electronic apparatus make null zero crossings nearly impossible to obtain, but zero crossings within a 50 keV energy range are considered reasonably minimized. Although, two point calibrations with ^{22}Na provide information on the energy distribution of incoming signals, the respective low-energy of decay peaks requires multiple calibration sources to be used.

Employing radioisotopes with larger photon energies in energy spectrum calibrations provide more accurate energy resolutions in the region of interest. Unfortunately, few radioisotopes release γ-rays naturally in the defined region of interest, 3 MeV - 6.5 MeV, making employment of ^{232}Th calibration sources essential. The ^{232}Th isotope decays with certain probability to ^{208}Tl with a 99% chance of β^- decay with an energy of 2614.5 keV [6]. Decay energies of ^{208}Tl are not in the desired region of interest, but give the highest possible calibration peak for available sources. To produce a calibration, a $\sim$5 minute measurement was taken with a single calibration source. A gaussian fit of the measured peak is used to record the centroid position and desired

energy assignment. From previous examples, a calibration entry of 511 keV would be assigned to the centroid position of the positron annihilation peak measured from the ^{22}Na calibration source, with the desired centroid position around channel 295. Calibration sources with more than one recognizable decay peak require multiple entries in to the calibration table. Presented in this study, a 6 point calibration was achieved through decays of ^{22}Na, ^{60}Co, ^{137}Cs, and ^{232}Th sources. Upon completion of the calibration, peak positions are verified with a brief ^{22}Na measurement.

Morning calibrations provided a consistent starting point for daily standoff measurements. Furthermore, initial passive background measurements provide a baseline background measurement for activation comparisons. After initial morning passive measurements, active interrogation measurements proceed depending on experimental criteria of the day. The presented experimental campaign consisted of three full days of active interrogation measurements. Active measurements were taken for $\sim$10 minutes for individual target materials with beam parameters consisting of a 2 s interrogation cycle. As discussed in the introduction, the interrogation cycle provides a pulsed (on/off) structure for accurate detection of active measurement signals. By radiating target material for one second, then allowing de-excitation processes to occur the next second, NaI detectors are able to measure desired signals associated with induced fission signatures. Without the "off" measurement period, detection of decay signals would be drowned out by accelerator bremsstrahlung beam interactions. Timing of the irradiation marker were recorded allowing data analysis software to isolate γ-ray signals produced during "off" inspection periods. Proceeding all active measurements, inspection object placement was verified using a two dimensional diode beam scanner provided by Idaho Accelerator Works. Similar to active measurements, PITAS provides a 60 Hertz bremsstrahlung photon beam which is then collected by a diode array within the beam scanner. Using a beam scanner to characterize the beam spot size at inspection object distances insures that bremsstrahlung photon beams will interact with the desired inspection object shown in Figure 3.8. Passive measurements were generally taken after a series of active measurements for a duration of 30-40 minutes. Passive measurement durations were longer than typical standoff measurement procedures due to activation analysis. Longer passive back-

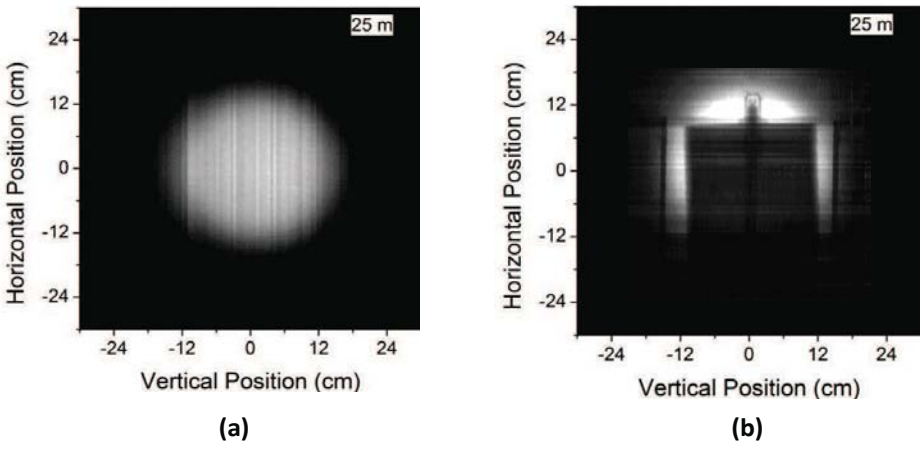

Figure 3.8: Beam Profile and Target Scan. Two beam scans from the Idaho Accelerator Works 120 diode translation array. Figure (a) shows a beam spot at 25 meters from the accelerator with vertical and horizontal positions reflecting the positioning of scanner. Figure (b) Beam scan with a Pb inspection object placed in the beam at 25 meters for a typical standoff measurement.

ground measurements are required to see decay processes within activated detectors. Although, active and passive measurements are done consecutively, pauses between measurements are required for inspection placement, exchanges of the control detector, alterations to shielding configurations and verification with the beam scanner. Furthermore, measurement data is immediately analyzed to insure measurement consistency and to provide greater understanding of detector performance. Finally, all experimental campaign days end with a passive measurement with durations greater than 30 minutes, allowing for comparisons with earlier passive measurements.

3.3.3 Data Analysis

Data analysis preformed outside of the initial experimental campaign seek to provide accurate comparisons regardless of detector calibration fluctuations. Each detector is calibrated individually and drifting within detector measurements can occur

due to responses to temperature fluctuations. Unfortunately, data analysis with calibration corrections are too time consuming to be performed real time with standoff measurement campaigns. The energy scale placed on the x-axis to denote the energy of detected particles, with yields of detected particles are shown on the y-axis in log form. Detection yields represent all particles detected within an active measurement, including those not consistent the timing region of interest. Further data analysis is employed with the use of a basic C++ programs to isolate detected particles in the desired energy region of 3 MeV - 6.5 MeV and desired timing region of $t > 250$ ms. The energy region of interest pertains to the characteristic decay energies released in the induced fission process. By filtering detected particles with energies lower than 3 MeV, greater sensitivity can be achieved due to the excess of low energy γ-rays detected that do not pertain to the signatures released within induced fission decay processes. Similarly, the time region of interest removes γ-rays received during the first 250 ms of the "off" period, accounting for the neutron thermalization processes described in chapter 2. Without this time region of interest, particle detection rates would be too large to distinguish induced fission signals released by the inspection object. Measurement data is provided to MPANT software in LST file format that includes a time stamp of particle interactions, calibrations for individual detectors, and the channel assignment of the detected particles.

All methods of data analysis require corrections to detector calibrations to insure accurate comparisons. Furthermore, proper normalization of corrected data is required to compare passive and active data sets. Detector calibration corrections alter the energy per bin width of individual detectors to achieve accurate ^{232}Th peak centroid placement at approximately 2614.5 keV. The ^{232}Th peak position is utilized due to its observable peak in both active and passive measurements, and its proximity to the desired energy region of 3 MeV-6.5 MeV. Once calibration corrections for an individual detector in an single measurement are obtained, corrections are then implemented in all data analysis processes. Data analysis consists of three methods time histograms, energy histograms and time incremented energy histograms.

Time histograms provide a particle detection yield as a function of the inspection time. Time histograms are normalized to show the rate of particle detection

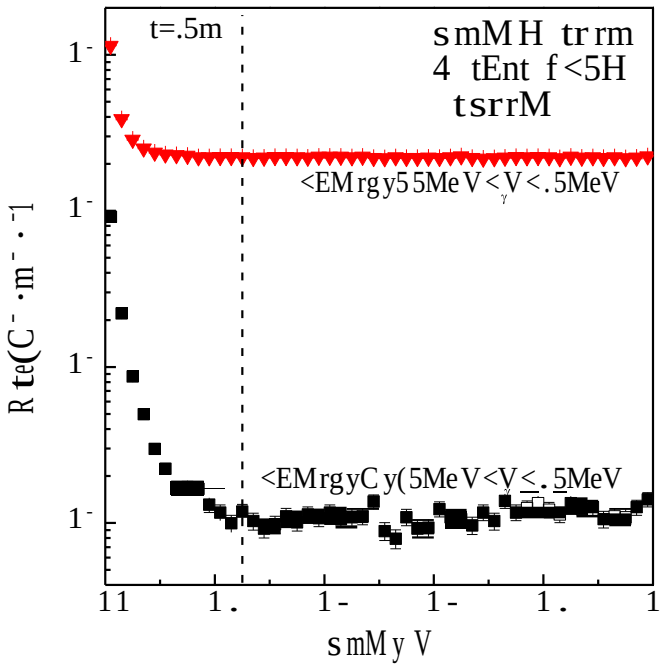

Figure 3.9: Time Histogram Comparison. Normalized detection rates of standard standoff measurement are shown during the 1 second "off" period of the inspection cycle for all energies and particles detected with energies within the energy region of interest.

within the 1 s "off" detection period. Time histograms are refined by isolating only the detected yields for energies within the desired region of interest 3 MeV to 6.5 MeV, known as an "energy cut". Isolating detected energies to the region of interest provides comparisons of shielding configurations, and confirms $t > 250$ ms timing strategies to mitigate (n,γ) produced in thermalization processes. A comparison of active measurement time histograms for a shielded NaI detector are shown in Figure 3.9. The $t > 250$ ms timing threshold is identified by the decreasing yield of detected particles produced in (n,γ) interactions after induced fission signatures are released. Therefore, desired signatures produced by inspection objects are more easily identified within the $t > 250$ ms timing window and decay processes for fissionable materials may be easier to see within desired energy regions. This is further reflected when detection rates are isolated to the 3 MeV - 6.5 MeV energy region seen in the "energy cut" time histogram. In contrast, total detected yields for all energies has a

significant increase in particle yields throughout the time. Detection rates are normalized by dividing detected particle yields by the surface area of the detector, the total charged received during the active run and the time bin of the time histogram.

Energy histograms provide detected particle yields as a function of particle energy. Energy histograms provide similar information to that produced by MPANT spectra software, but also include refining particle detections to the those received after the $t > 250$ ms threshold discussed above. Known as "time cuts", energy histograms can show the particle yields within the desired energy region of interest after the initial 250 ms thermalization period when (n,γ) interactions occur. Shown in Figure 3.10,

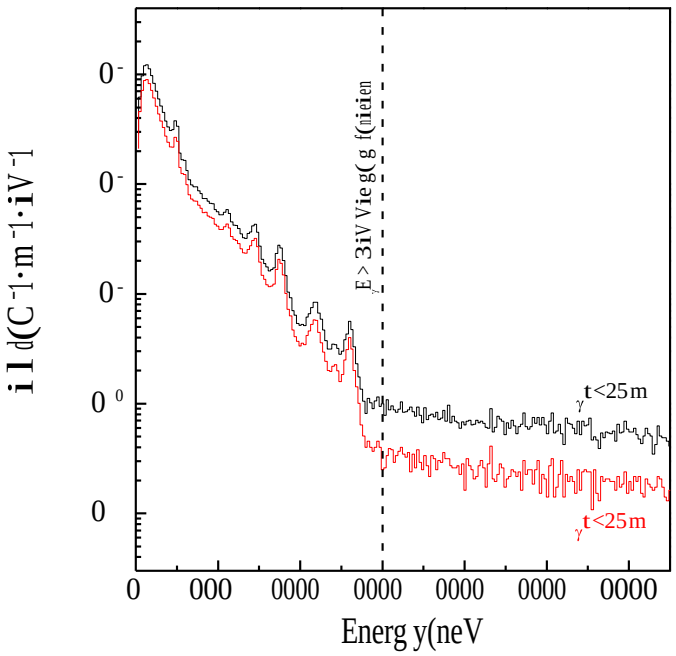

Figure 3.10: Energy Histogram Comparison. Normalized particle yields as a function of particle energy. Particle yields are presented for the total duration of the 1 second "off" period and for the time region of interest $t > 250$ ms.

two energy histograms for a shielded NaI detector during a NOI active measurement are compared. The spectra represent the particle detection yields as a function of their energy during the entire 1 second "off" inspection cycle. Time cut spectra consist of the particles detected after the 250 ms decay period, which naturally has a decrease of detected particles from yields observed for the entire 1 second "off" pe-

riod. Comparison of the energy histogram reveals that active signals increased if the full duration of the inspection period is considered, this increase in counts is due to (γ,n) and (n,γ) interactions produced from the photon interactions with the inspection object and surrounding environment. Neutrons undergo thermalization as they interact with the surrounding environment, loosing energy until absorption occurs. Upon absorption, an (n,γ) interaction occurs releasing a high-energy γ-ray into the local environment that can effect standoff measurement accuracy. This increase is further reflected in the energy region of interest shown after the dotted line placed at 3 MeV.

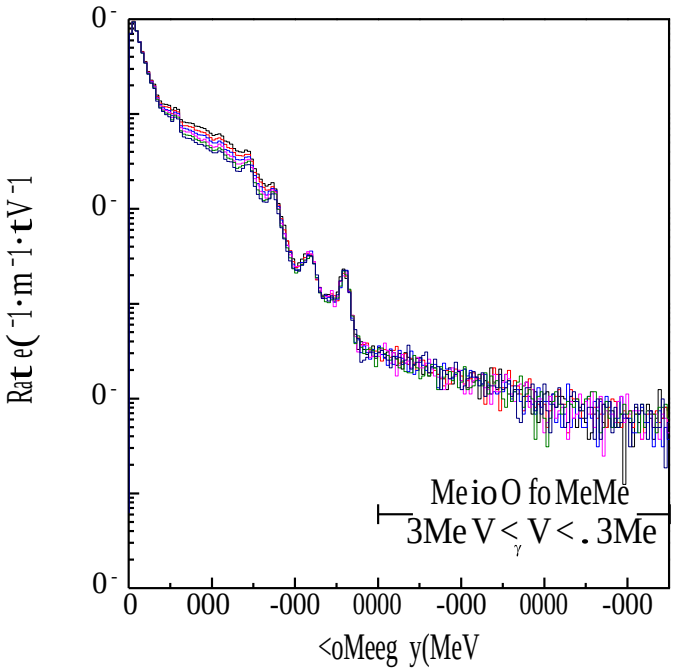

Figure 3.11: Waterfall Data Analysis. A waterfall spectra of the unshielded NaI detector after an active Pb measurement. The passive measurement is split into 5 minute time bins with each line representing 5 minutes of the passive measurement.

Time incremented energy histograms provided particle yield measurement analysis similar to energy histograms, but break histogram measurements into time bins for measurement evolution comparisons. Particularly useful for detector activation analysis, time incremented cuts break apart energy histograms into regular time intervals. For example, a sample waterfall plot is shown in Figure 3.11 with time bin

designations of 5 minutes. Utilized for passive measurements, waterfall cuts produce a 5 minute snap shot of detector yields, producing comparable time evolution of detector activity. Data analysis shows the decay of activated isotopes within the NaI detectors, and provide insight on performance of varying shield configurations. Decreases in particle detection between 5 minute bin durations can give information on activated isotope identities. The waterfall time bin durations can be changed at the preference of experimental personnel allowing further exploration of activated isotope decay rates. Specifically, the presented example incremented histogram shows the unshielded passive background received directly after an active Pb measurement. The increase in measured particles is a result of neutron absorption within the NaI detector received from neutrons emitted during induced fission process in the inspection object.

Data analysis techniques attempt to correct fluctuations within calibrations of individual detectors, providing accurate comparisons of measurements in histogram and waterfall analysis. Although, calibration corrections increase data compatibility, uncertainties from calibrations do exist. Detector calibrations were often performed during the early morning, making NaI detectors specifically susceptible to thermal fluctuations. As temperatures increased throughout the day, drifting was observed within the peak placements of individual detectors. When properly corrected, uncertainties caused by these fluctuations can be avoided but never completely mitigated. Furthermore, uncertainties lie within uniformity of inspection object distances and concurrent measurements with activated detectors. While these errors do play a significant role in standoff detection methods, detection of inspection objects were not negatively impacted by uncertainties in the experimental environment.

Chapter 4

Results

Shielding configurations analysed during the November 2012 campaign confirmed a significant reduction of detector activation within NaI crystals. Multiple shielding configurations were used, however, a majority of measurements were taken with 4 inch borated polyethylene shielding with a thin layer of cadmium between the polyethylene and detector. Characterization of optimum shielding configurations for NaI γ-ray detectors was achieved through initial passive background comparisons and shielding thickness investigations.

Data analysis begins with understanding the initial conditions of the individual NaI detectors. Comparisons of the first passive background measurement confirm the consistent initial conditions of unshielded and shielded NaI detectors. While the shielding configuration's suppression of natural background signals is observed in Figure 4.1, consistent performance of control and unshielded detectors assures accurate measurement comparisons later in the experimental campaign. Active measurement energy histogram comparisons displayed the undesired signals associated with detector crystal activation. In contrast, detector activation was mitigated for the shielded NaI detectors depending on shielding configuration thickness. Specifically, detection rate comparisons between experimental campaign days reveals an increase in activation for thinner shielding configurations. All detectors experienced some activation, however only unshielded detectors showed evidence of activation within the energy region of interest.

4.1 Initial Passive Background Comparisons

Initial passive background measurements provide insight on the starting conditions of the detector apparatus as well as identifying natural passive background levels within the experimental environment. These natural background levels are then used through shielding configuration comparisons and activation analysis for all detectors present. The first passive measurement was conducted on November 12th,

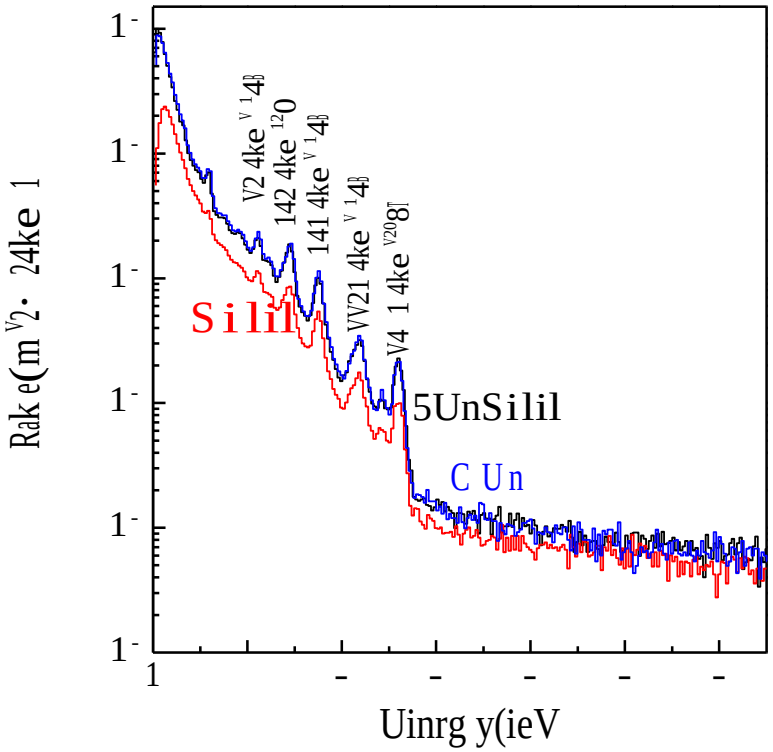

Figure 4.1: Initial energy histogram comparison. Energy histograms compare normalized yields to the energy of the detected particle. Displayed are the energy histograms of all NaI detectors for the initial passive measurement of the experimental campaign. Detector NaI 1 and the control detector (NaI 3) were unshielded, while NaI 2 had a 10.2 borated polyethylene and cadmium shielding configuration.

2012 before any active measurements were conducted. These measurements were conducted after source calibrations described previously in the experimental section. A decrease in the particle detection rate due to shielding is observed for initial passive measurements seen in Figure 4.1. Detector performance is consistent with previ-

ous experimental campaigns, with the energy histograms reflecting the characteristic natural passive background observed in the IAC airport facility experimental environment. Unshielded and control respective spectra are near identical, confirming initial conditions of unshielded detectors. Peaks identified within passive spectra represent the passive signals received from terrestrial radiation with the experimental spectra. While a majority of these peaks are products of the uranium and thorium decay chain, other peaks such as ^{40}K also occur naturally in the experimental environment. Furthermore, the expected decrease in photon detection rates for shielded NaI detectors is observed in all energy regions. While changes are seemingly insignificant, even minimal decreases in this region of interest can improve standoff measurement sensitivity.

4.2 Shielding Comparisons

Although, multiple shielding configurations were explored within the experimental campaign, a majority of measurements were done with a 10.2 cm borated polyethylene layer with a thin layer of cadmium between the polyethylene and detector crystal. The experimental strategy was to begin with the thickest shielding possible to prevent activation within the shielded detector. Energy histograms for the unshielded detector are shown below in Figure 4.2. Individual histograms represent a single active measurement consisting of a no inspection object, Pb, or ^{238}U inspection object. Active background signals observed in energy histograms for the unshielded detector showed significant γ-ray detection throughout the energy region. Within the energy region of interest active measurement signals are prevalent out to $\sim$5 MeV, where active spectra align with initial "natural" passive measurements shown in the previous section. As desired, the ^{238}U active measurement signal produces γ-ray yields throughout the energy region of interest. In contrast to shielded measurements, activation through neutron absorption was observed in energy histograms of the unshielded NaI detector. Increases in photon yields between no inspection object(NIO) and Pb inspection object exemplify the possibility of activation in each measurement measurements. In Figure 4.3, identical active measurements as those in Figure 4.2 are shown for the

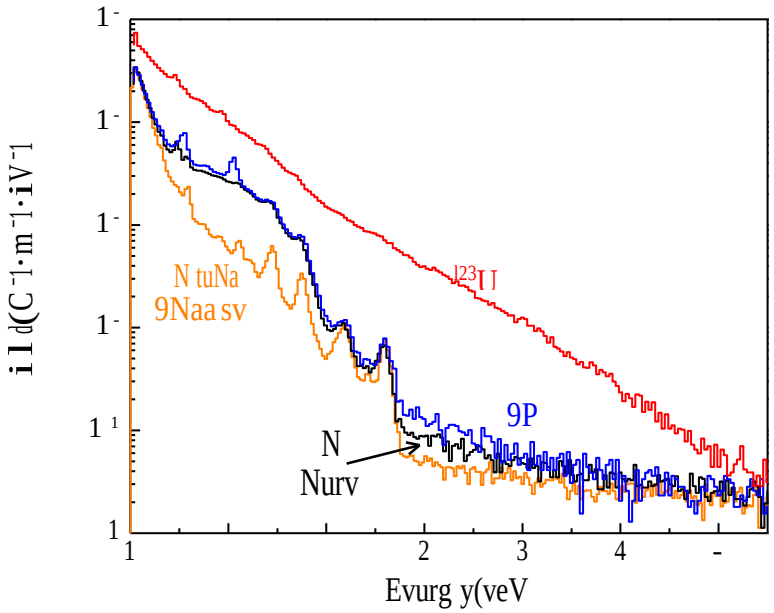

Figure 4.2: Unshielded energy histogram comparison. Active measurement comparison are shown for the unshielded detector with initial natural background measurement. Active measurements are shown for No target, Pb and ^{238}U inspection objects with a 60 Hz photon beam and measurement duration of ~10 minutes.

shielded detector. Activation is not observed in consecutive NOI and Pb inspection object measurements. Although, a small signal from the Pb inspection object is visible in the low-energy region of the histogram, active measurement signals are consistent with initial "natural" passive levels for energies greater than ~2 MeV, implying little activation with the detector crystal. Peaks appearing in Pb spectra pertain to metastable states of ^{208}Pb during active interrogations by (γ,n) reactions. Specifically ^{207m}Pb states observed release characteristic decay emissions of 570 keV and 1063 keV γ-rays. Further comparisons of active measurements are depicted in Figure 4.4 with time histograms showing the rate of detection for unshielded and shielded NaI detectors. Further confirmation of the shielding configuration performance are observed in the shielded detector time histogram. In contrast to unshielded detection rates, shielded rates within the energy region of interest returned to initial passive measurement levels. Isolating detection rates within the energy region of interest provides greater evidence for a decrease of activation within the shielded detectors.

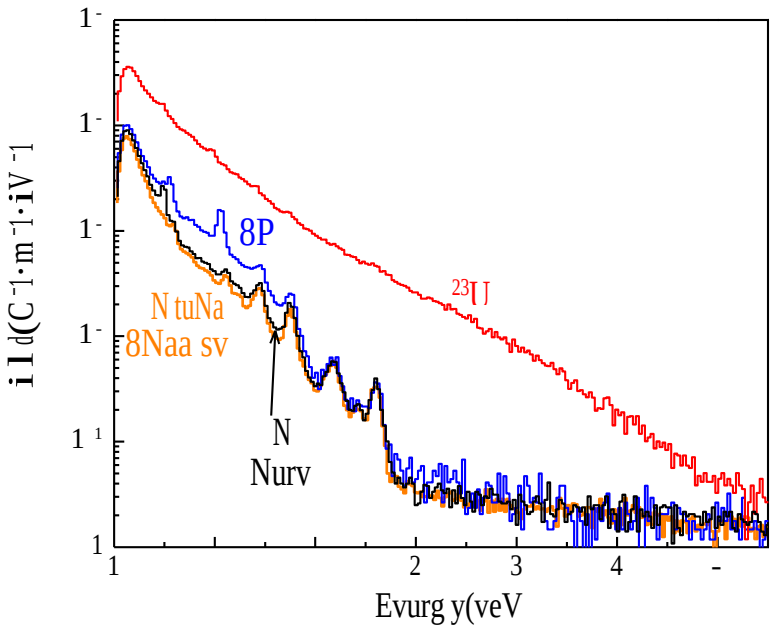

Figure 4.3: Shielded energy histogram comparison. Active measurement comparisons are shown for the shielded detector with 10.2 cm of borated polyethylene and a thin layer of cadmium between borated poly and detector crystal. Active measurements are shown for No target, Pb and ^{238}U inspection objects with a 60 Hz photon beam and ~10 minute measurement duration.

Activation observed within the energy region of interest, as seen in unshielded rates and spectra, can decrease standoff detection sensitivity.

Detection rates for ^{238}U measurements are pronounced regardless of shielding configuration, therefore, signatures within the active signal produced by ^{238}U standoff measurements will be detected at greater distances. However, extraneous signals produced through activation decay processes will decrease accuracy of consecutive measurements. NIO and Pb measurements provide a baseline of active measurement background signals produced from the PITAS system and the surrounding environment.

Although, comparisons of the 10.2 cm borated polyethylene and cadmium shielding configurations showed remarkable activation protection, holding none fissile inspection objects spectra to near natural background levels, measurements of thicknesses less than 10.2 cm were investigated for similar shielding performance. Shielding

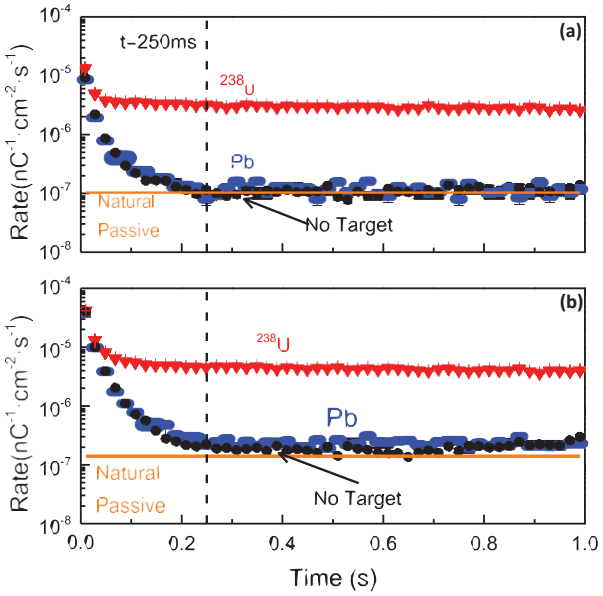

Figure 4.4: Active time histogram comparison. Time histograms for active measurements with Pb, No Target and ^{238}U inspection objects within energy region of interest 3 MeV - 6.5 MeV are shown for the shielded(a) and unshielded(b) NaI detectors.

configuration thickness comparisons are presented in Figure 4.5, with shielding configurations consisting of; 10.2 cm of borated polyethylene with cadmium layer, 5.1 cm of borated polyethylene with cadmium layer, 10.2 cm borated polyethylene with no cadmium and only cadmium. Resulting energy histograms show an increase of detection yields as the borated polyethylene shielding configurations thicknesses decrease. Thinner shielding configurations did not suppress detector activation, causing photon detection spectra to never return to initial passive background measurements as observed in 10.2 cm thick shielding configurations. Significant differences of active signals were not observed with 10.2 cm thick borated polyethylene and cadmium, when compared to similar shielding configurations without cadmium. Active

measurements for various shielding configurations were done in near succession, but inaccuracies of energy histogram data could be present due to detector activation. Detector activation analysis investigated the detection rates in passive measurements immediately following active measurements with shielding configurations of different thicknesses. Detection rates presented reflect an increase in activation for thinner borated polyethylene configurations, concluding in an optimum shielding thickness of approximately 10.2 cm of borated polyethylene.

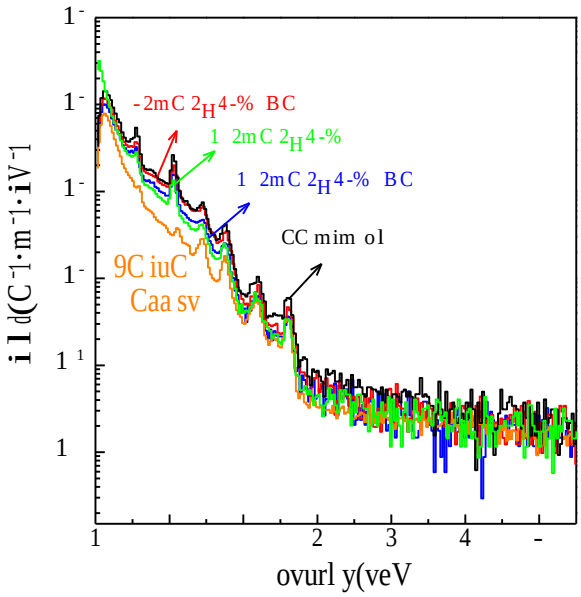

Figure 4.5: Thickness energy histogram comparison. Energy histograms isolating γ-ray detection for times greater than 250 ms within the "off" period of the inspection cycle are presented with multiple shielding configurations for a Pb inspection object. Active measurements utilized a 60 Hz photon beam with a 1 sec on/1 sec off inspection cycle for durations of ~10 minute durations.

4.3 Activation Analysis

Activation was observed within all detectors after consecutive active measurements were conducted. Shielded detectors activated, however activation was isolated to low-energy γ-rays. Time incremeneted energy histograms provide comparisons of γ-ray spectra within a designated time interval allowing for observation of radioisotope de-

cay within the detector crystal or experimental environment. For the waterfall spectra presented below, 5 minute intervals were used to monitor decay processes within a detector. Waterfall energy histograms in Figure 4.6 and Figure 4.7 compare the ini-

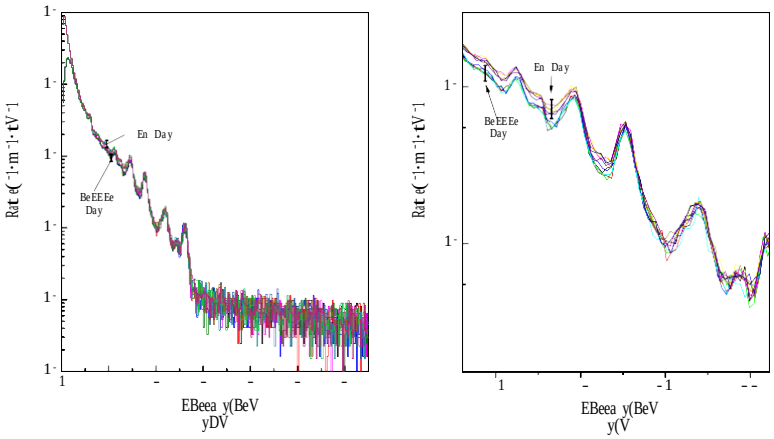

Figure 4.6: Shielded time incremented energy histogram comparison. Waterfall energy histogram measurements for a shielded NaI detector.Separated into 5 minute time bins, each waterfall spectra depicts the detection yields of γ-rays within a 5 minute duration. Waterfall(a) is the waterfall energy histogram for all energies. Waterfall(b) is a magnified view of the low-energy region of waterfall spectra where initial and final waterfalls are shown with greater detail.

tial passive measurements discussed in section 4.2, and the end of the day passive measurement conducted after daily active measurements occurred. By comparing waterfall energy histograms with initial detector conditions versus those measured at the end of the day characterization of the activation accumulated through out a typical experimental campaign is possible. Measurements for the shielded detector are presented in Figure 4.6, showing some activation during the first day of the experimental campaign. Slight inconsistencies within histograms may exist due to non-identical shielding configurations for active and passive measurements. Specifically, cadmium was removed from the 10.2 cm borated polyethylene shielding configuration for shielding thickness comparisons but was not returned to the shielding configuration for the end of day passive measurement. Furthermore, activation within the shielded detector accumulated during thickness studies could affect end of day passive measurements. However, end of the day passive measurements for the shielded

detector are near identical to beginning passive measurements, requiring a secondary plot to show differences in spectra at lower-energies (Figure 4.6b). Within the low-

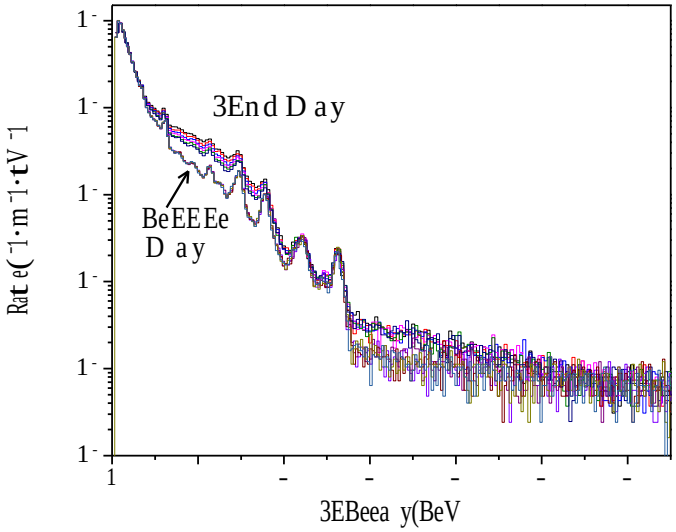

Figure 4.7: Unshielded time incremented energy histogram comparison. Waterfall energy histograms with time durations of 5 min are compared for passive measurements taken at the beginning and end of the first day in the experimental campaign.

energy region shown in the magnified view, decay processes of low-energy isotopes were observed, most likely associated with activated ^{128}I nuclei within the detector crystal. Further evidence of activation is seen in the unshielded waterfall energy histograms shown in Figure 4.7. In contrast to the shielded detector, activation is not only seen within the low-energy region attributed to activation of ^{128}I but activation is also observed within the high-energy region of interest. Activation within the higher regions suggest an activated isotope with a higher Q value such as ^{24}Na. Evidence for the activation of ^{24}Na isotopes within the crystal is seen in the lack of activation beyond 5 MeV, relating to the maximum Q value of the ^{24}Na decay processes. Initial measurement histograms coincide with those of the shielded detector, displaying waterfall spectra lying on top of one another. This lack of "broadness" reflects minimal decays processes occurring within the detector crystals, confirming detectors initially had no activation. Even with minimal activation, as seen with the shielded detector, activated NaI crystals will detect decreasing rates for each consecutive 5 minute measurement, coinciding with the decay process previously described.

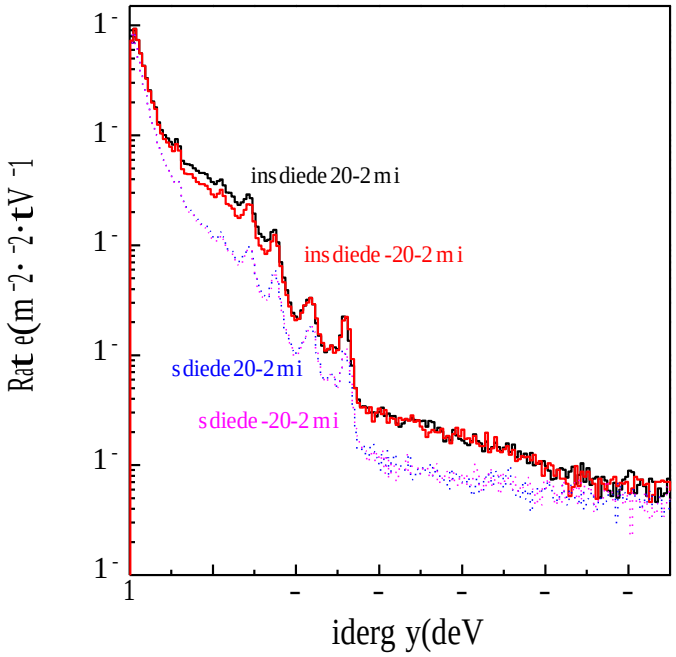

Figure 4.8: 20 Minute incremented energy histogram comparison. A comparison of shielded and unshielded waterfall energy histograms for end of day passive measurements with 20 minute time intervals. Solid curves represent the detection yields for the unshielded detector broken in to 20 minute intervals. Similarly, detection yields for end of day passive measurements for the shielded detector are shown with dashed curves. Passive measurements were conducted with no inspection object for durations of ~40 minutes.

Activation of the unshielded detector becomes more prevalent when energy histograms are conducted for large time intervals as shown in Figure 4.8. Further evidence of activation of ^{24}Na and ^{128}I nuclei within the unshielded NaI detector is shown in Figure 4.8. Utilizing 20 minute time bins for the waterfall spectra allows for greater scrutiny of decay processes within the activated detectors. Decay processes are observed within the low-energy region of the histogram, suggesting the decay processes associated with ^{128}I nuclei. Activation is also observed within the high-energy region of interest associated with ^{24}Na isotopes. Although, the shielded waterfall energy histograms depict little to no activation within the detector crystal agreeing with 5 minute waterfall analysis above, activation within the shielded detector becomes apparent through detection rate analysis. In Figure 4.9 the detection

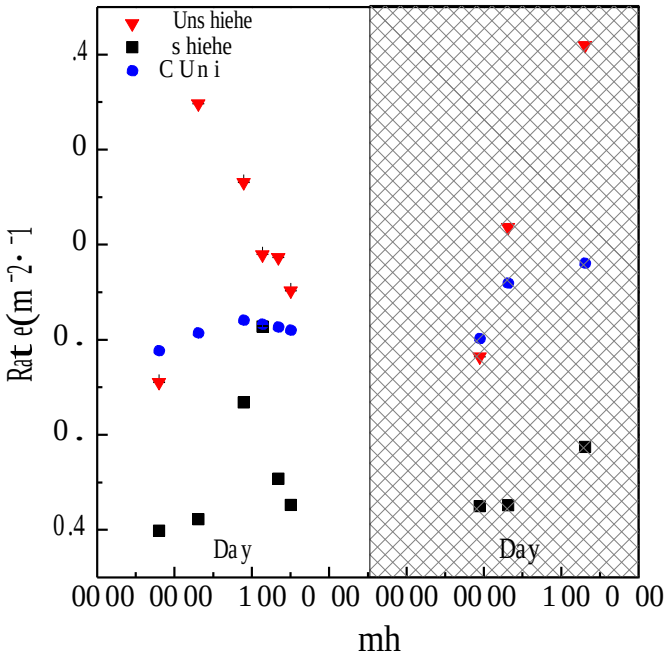

Figure 4.9: All energy detection rate comparison. Passive measurement detection rates for unshielded(T), shielded(•) and control(•) detectors for the first and second day of the experimental campaign. Passive measurement durations ranged from 20-40 minutes with no inspection objects present. Detection rates reflect the detected particles within total energy region after the initial 250 ms within the 1 second "off" period of the inspection cycle.

rates for unshielded, shielded and control NaI detectors are shown for passive measurements conducted during day 1 and 2 of the experimental campaign. The data show the detection rates for all energies within the passive measurement. Between each passive measurement a series of active measurements was conducted allowing for activation within detectors. Shielded detector rates increased as shielding configurations were reduced for the thickness studies discussed in section 4.2. The increase in detection rate observed in the 3rd and 4th passive measurements coincided with the 5.1 cm borated polyethylene shielding configuration measurement and the cadmium only shielding measurement respectively. A reduction of detection rate occurs in the 5th passive measurement reflecting a return to the 10.2 cm borated polyethylene shielding configuration. During the first day of the campaign an increase of 13.6% was observed in the shielded detector from the initial morning passive measurement

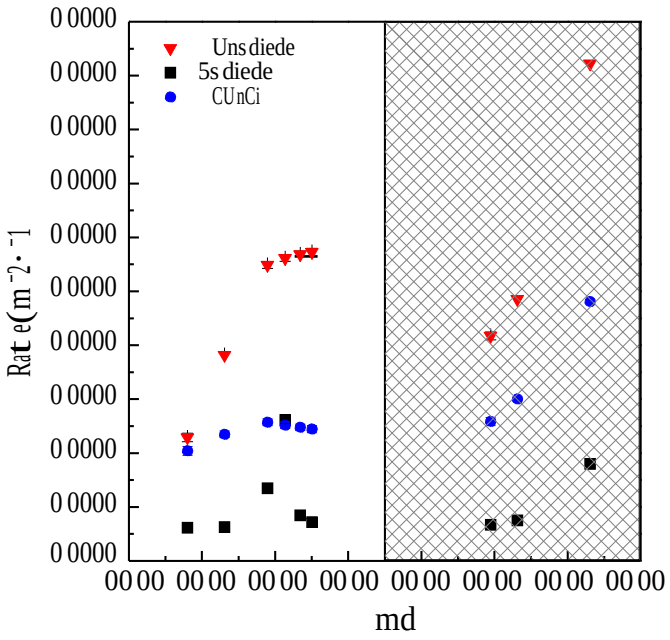

Figure 4.10: High-Energy detection rate comparison. Passive measurement high-energy detection rates for unshielded(T), shielded(•) and control(•) detectors for the first and second day of the experimental campaign. Passive measurement durations ranged from 20-40 minutes with no inspection objects present. Detection rates reflect the detected particles within the high-energy region after the initial 250 ms within the 1 second "off" period of the inspection cycle

to the "end of day" the passive measurement. Detection rates returned to near initial conditions for the shielded detector, but a comparative increase was observed for the unshielded detector's intial passive measurements on the 2nd day. Regardless, evidence of shielded detector activation was seen in detection rates for the 2nd day of the campaign. Active measurements conducted in the second day primarily utilized the 10.2 cm borated polyethylene and cadmium shielding configuration, and consisted of mainly ^{238}U inspection objects. The final passive measurement shown in Figures 4.9 and 4.10 followed a 30 minute active ^{238}U measurement. The shielded high-energy detection rate increased 27.7% from initial passive background measurements done at the beginning of day 2 to the end of day passive measurements reflecting the activation acquired in the longer duration ^{238}U measurements.

Activation was observed within the high-energy region of interest for the un-

shielded detector in both campaign days, with a significant activation occurring on the 2nd campaign day coinciding with an increase of ^{238}U inspection object measurements and their durations. Characteristic activation is observed within the unshielded detector for both days, with a 54% and 35.8 % rate increases respectively. While large increases for day 2 rates are most likely contributed to the longer time duration ^{238}U measurements conducted, both daily increases reflect the cumulative nature of activation with the NaI crystal. Affects of prolonged ^{238}U active interrogations are also evident in the increased detection rates of both control and shielded detectors at the end of day 2. However, day 1 of the experimental campaign did show small increases within the shielded detector, these increases were more pronounced during day 2 due to the prolonged duration of activation measurements.

Once again, activation due to thinner shielding configuration investigations is observed within the detection rate analysis providing confirmation of the 10.2 cm borated polyethylene shielding configuration performance. Both detectors present throughout the active measurements conducted in the campaign can be compared with control detector passive measurements, however, inconsistency in control detector placement during active measurements is reflected in day 2 detection rates. For the first experimental campaign day, consistent detection rates were observed within the control detector, showing a minimal increase of 5.6% throughout the day. On the second day of the campaign, activation within the shielded detector was reduced to detection rate levels consistent with the control detector implying shared initial conditions of the unshielded and control detector discussed in initial background discussions. In contrast to the first day, the control detector may have not been placed far enough from the experimental environment to fully protect the scintillation crystal from activation. Rates for the control NaI detector increased 19.8% through campaign day 2, reflecting the exposure to the active experimental environment. Particle detection rates within the high-energy region of interest (3 MeV-6.5 MeV) reflected similar rate increases due to activation of the detector crystal.

Chapter 5

Conclusions

Experimental campaigns conducted in November 2012 investigated shielding configurations for NaI scintillation detectors for active inspection applications. The experimental campaign tested multiple shielding configurations for active background suppression as well as the shielding's ability to protect detector crystals from activation through neutron absorption. Shielding configurations utilized borated polyethylene of variable thicknesses and thin cadmium layers. Shielding configuration tests consisted of multiple passive background measurements and active measurements with no inspection object, Pb and ^{238}U inspection objects with durations of 20-40 minutes and 10 minutes respectively. Active and passive measurements were analyzed using time histograms, energy histograms and time incremented waterfall histograms. An optimum shielding configuration consisted of borated polyethylene and a thin layer of cadmium. Suppression of active signals caused by detector activation accumulated in Pb and no inspection object measurements was observed in the energy region of interest suppressed to initial passive background levels. Although some activation was observed within the shielded NaI detector, activation analysis through waterfall plots do not suggest significant decreases in standoff measurement sensitivity. However, the shielding configurations tested are intended for a large scale NaI γ-ray detector and utilitarian concerns altered desired shielding configurations.

5.1 Conclusions

Cadmium layers were removed from final panel designs due to concerns of material handling. Cadmium is a particularly hazardous material to work with and was deem unacceptable for final panel design. The final panel design utilized 10.2 cm of 5% borated polyethylene shielding configurations covering 16 NaI detectors identical to those in the presented campaign. The borated polyethylene alone weighed a remarkable 700 kg.

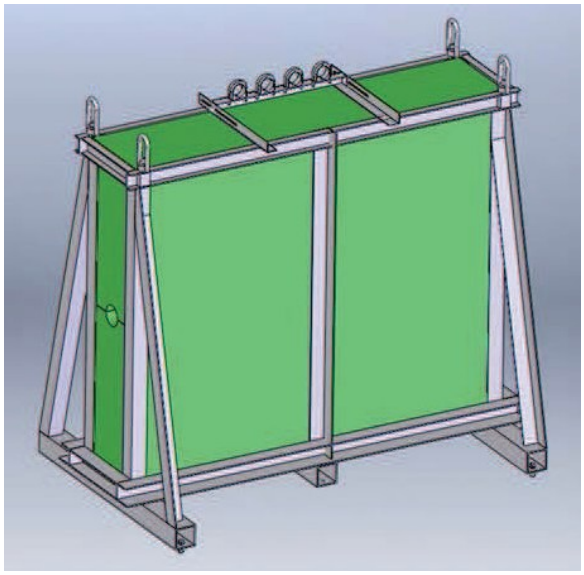

Figure 5.1: Final Panel Design. A schematic of final panel design utilizing borated polyethylene shielding. Detector consisted of aluminium detector frame (not shown), overlapping 10.2 cm borated polyethylene panels and a steel holding frame.

The final panel design consisted of an aluminum sleeve frame built for holding the NaI detectors, surrounded by a shielding configuration employing a series four 2.4 cm overlapping borated polyethylene panels. Shielding configurations were kept in place by a large steel frame with fork lift accessible footings. The total panel dimensions were 167.64 cm x 203.61 cm with a depth of 121.92 cm, with a total surface area of 0.66 square meters. Perspective standoff measurement capabilities for the finished panel are expected to exceed 50 meters.

5.2 Future Work

Although nearly a decade old, there are still many facets of standoff detection open for greater exploration. Utilizing a large surface area γ-ray panel such as the proposed detector panel in this study, may create new opportunities for standoff detection of fissile materials. Experimental campaigns conducted in the Spring of 2013 investigated the standoff detection capabilities of the large scale γ-ray detector. Although initial campaigns with the large scale panel were a success, a myriad of work is required to optimize system design and detection strategies of fissionable materials.

Avenues of future research include optimization of inspection cycles and beam parameters, veto counting background suppression and exploration of other induced fission signatures. Inspection cycle and beam parameter optimization are two simple places to gain sensitivity in measurements. Although increases in sensitivity may not produce substantial increases in distance capabilities, investigations of asymmetric inspection cycles coupled with higher bremsstrahlung beam rep rates could create more accurate measurement results. Research up to the current measurements have relied purely on the 1/1 s 1/1 off inspection cycles. Although, these inspection cycles have produced acceptable fission signatures within desired regions of interest, further exploration of inspection cycle configuration could yield greater sensitivity in standoff applications. By allowing inspection objects to be irradiated for longer period of time, for example 2 seconds, induced fission signatures may be stronger than with shorter irradiation times. Variations within both irradiation and measurement periods could produce more sensitive standoff measurements.

Similarly, veto background counting could produce significant decreases in cosmic radiation detected in passive background signals. Shielding configurations presented in this study are passive in nature, utilizing active shielding methods may assist by further suppressing background signals without negating desired fissionable signatures. Active shielding techniques are often used for large scale particle catching applications, but utilizing time based veto counting could be applicable for small standoff measurement systems. Utilizing known characteristics of incoming particle, detectors placed on top of detector, nadir to incoming cosmic signals, can read

times of particle interaction with the top of the panel. Detection times determined to align with cosmic particles can be vetoed from total signal measured. This method could reduce passive background levels drastically without requiring massive high z shielding configurations.

Finally, significant research into the measurement of prompt fission signatures hangs higher on the standoff measurement tree. Standoff measurement strategies that utilize prompt neutron signatures may increase standoff measurement capabilities to farther distances than previously achieved. The comparative signal produced from prompt neutrons is drastically larger(nearly 7 times) than delayed signatures. However, difficulties do come with such potential, as timing constraints on detector resolution and more complex processing electronics become crucial hurdles for prompt neutron detection. Regardless of complications, the shear magnitude of prompt signals makes them extremely enticing for standoff measurement research. As accelerator endpoint energies increase, interferences with the experimental environment material may occur more frequently. Utilizing prompt signatures may allow for further standoff distances to be achieved, while still retaining current accelerator parameters.

Bibliography

[1] Quadrennial defense review report. Technical report, Department of Defense, February 2010.

[2] Federal Technology Agency.

[3] Edna S. Cardenas. Developing signatures for bgo. Master's thesis, Idaho State University, 2011.

[4] Mario Conte and William W MacKay. *An Introduction to the Physics of Particle Accelerators*. World Scientific Press, 2008.

[5] Ashok Das and Thomas Ferbel. *Introductory Nuclear and Particle Physics*. John Wiley and Sons Inc., 1994.

[6] R.B. Firestone and L.P. Ekström.

[7] Claus Grupen and Boris Shwartz. *Particle Detectors*. Cambridge University Press, 2008.

[8] Mathew Thomas Kinlaw. Delayed neutron group parameters from photofission, 2007.

[9] Glenn F. Knoll. *Radiation Detection and Measurement*. John Wiley and Sons, 2000.

[10] Kenneth S. Krane. *Introductory Nuclear Physics*. John Wiley and Sons Inc., 1988.

[11] Edward Thomas Elzea Reedy. Discrete /grays/ from photofission for nuclear forensics applications. Master's thesis, Idaho State University, 2011.